

# Neural Closure Models for Dynamical Systems

Abhinav Gupta\*<sup>1</sup> and Pierre F.J. Lermusiaux<sup>†1</sup>

<sup>1</sup>Department of Mechanical Engineering, Massachusetts Institute of Technology,  
Cambridge, MA 02139

Sunday 17<sup>th</sup> July, 2022

## Abstract

Complex dynamical systems are used for predictions in many applications. Because of computational costs, models are however often truncated, coarsened, or aggregated. As the neglected and unresolved terms along with their interactions with the resolved ones become important, the usefulness of model predictions diminishes. We develop a novel, versatile, and rigorous methodology to learn non-Markovian closure parameterizations for low-fidelity models using data from high-fidelity simulations. The new *neural closure models* augment low-fidelity models with neural delay differential equations (nDDEs), motivated by the Mori-Zwanzig formulation and the inherent delays in natural dynamical systems. We demonstrate that neural closures efficiently account for truncated modes in reduced-order-models, capture the effects of subgrid-scale processes in coarse models, and augment the simplification of complex biochemical models. We show that using non-Markovian over Markovian closures improves long-term accuracy and requires smaller networks. We provide adjoint equation derivations and network architectures needed to efficiently implement the new discrete and distributed nDDEs. The performance of discrete over distributed delays in closure models is explained using information theory, and we observe an optimal amount of past information for a specified architecture. Finally, we analyze computational complexity and explain the limited additional cost due to neural closure models.

**Keywords**— delay differential equations, reduced-order-model, turbulence closure, ecosystem modeling, data assimilation, machine learning

## 1 Introduction

Most models only resolve spatio-temporal scales, processes, and field variables to a certain level of accuracy because of the high computational costs associated with high-fidelity simulations. Such truncations of scales, processes, or variables often limit the reliability and usefulness of simulations, especially for scientific, engineering, and societal applications where longer-term model predictions are needed to guide decisions. There are many ways to truncate high-fidelity models to low-fidelity models. Examples abound and three main classes of truncations are: evolving the original dynamical system in a reduced space, e.g., using reduced-order-models (ROMs) [17, 91, 68, 44]); coarsening the model resolution to the scales of interest [51, 28, 2, 80]; or reducing the complexity or number of state variables, components, and parameterizations [53, 14, 92]. In many applications, the neglected and unresolved terms along with their interactions with the resolved ones can become important over time, and researchers have developed a variety of modeling techniques to represent the missing terms. Techniques that express these missing terms as functions of modeled state variables

---

\*guptaa@mit.edu

<sup>†</sup>pierrel@mit.edu (Corresponding author.)

and parameters are referred to as closure models. A main challenge is that no one closure approach to date is directly applicable to all three main classes of model truncations. Another challenge is that closure models are only well-defined for either linear problems or simple cases. Finally, they can easily become ineffective in the face of nonlinearities.

Due to the explosion of use of a variety of machine learning methods for solving or simulating dynamical systems, a number of data-driven methods have been proposed for the closure problem. Most of them attempt to learn a neural network as the instantaneous map between the low-fidelity solution and the residual of the high- and low-fidelity solution, or their residual dynamics [66, 89, 90, 81]. They often use recurrent networks such as long-short term memory networks (LSTMs), gated recurrent units (GRUs) etc., with justification based on the Mori-Zwanzig formulation [85, 18, 33], and embedding theorems by Whitney [93] and Takens [86]. These approaches do not however take into account errors in the time evolution of the state in the presence of neural-networks during training. Moreover, one requires either access to the equations describing the high-fidelity model or frequent enough high-fidelity data to be able to compute the time derivative of the state with high level of accuracy. Such requirement on the training data might be a luxury in a lot of scenarios. The requirement of very frequent snapshot data of the system is also true for methods which achieve model discovery using sparse-regression and provide interpretable learned models [12, 42]. These issues are addressed by using neural ordinary differential equations (nODEs; [16]) and some researchers recently used nODEs for closure modeling. Some directly learn the ODE system from high-fidelity simulation data without using the available low-fidelity models [58], which could lead to the requirement of bigger neural networks. Others combine nODEs with model discovery using sparse-regression [95] or only learn the values of parameters in existing closure models [67]. Nearly all the studies in the existing literature primarily only attempt to address the closure for ROMs. Finally, the existing machine learned closure models are not yet used for long-term predictions, i.e. forecasting significantly outside of the time-period to which the training data belonged to.

In the present study, we propose a new neural delay differential equations (nDDEs) based framework to learn closure parameterizations for low-fidelity models using data from high-fidelity simulations and to increase the long-term predictive capabilities of these models. Instead of using ODEs, we learn non-Markovian closure models using DDEs. We base the theoretical justification for using DDEs on the Mori-Zwanzig formulation [85, 18, 33] and the presence of inherent delays in many dynamical systems, especially biological systems [32, 87]. We refer to the new modeling approach as *neural closure models*. We demonstrate that our methodology drastically improves the predictive capability of low-fidelity models for the three main classes of model truncations. Specifically, our neural closure models efficiently account for truncated modes in ROMs, capture the effects of subgrid-scale processes in coarse models, and augment the simplification of complex mathematical models. We also provide adjoint equation derivations and network architectures needed to efficiently implement nDDEs, for both discrete and distributed delays. We further investigate the impacts of using no-delays, discrete-delays, and distributed-delays in closure models, and argue their relative performance based on information theory, along with changing the amount of past-information being included. Our first two classes of simulation experiments utilize the advecting shock problem governed by the Burger’s partial differential equation (PDE), with its low-fidelity models derived either using proper-orthogonal-decomposition Galerkin projection [5] or reducing the spatial grid resolution. Our third class of experiments consider marine biogeochemical models of varying complexities [63, 25, 10], with low-fidelity models obtained by aggregation of components and other simplifications of ecosystem processes and parameterizations. Finally, we analyze computational complexity and explain the limited additional computational cost due to the presence of neural closure models.

## 2 Closure Problems

The need for closure modeling in dynamical systems arises because of a variety of reasons. The reasons often involve computational costs considerations, but also include the lack of data to resolve complex natural processes, the limited understanding of fundamental dynamics, and the inherent nonlinear growth of uncertainties due to model errors and predictability limits [e.g. 76, 49, 48, 7, 77]. In this section, we examine the three main classes of low-fidelity models that can require closure modeling.

## 2.1 Reduced Order Modeling

Let us consider a nonlinear dynamical system with state variable  $u \in \mathbb{R}^N$  and the full-order-model (FOM) dynamics governed by,

$$\begin{aligned} \frac{du(t)}{dt} &= Lu(t) + h(u(t)) \\ u(0) &= u_0, \end{aligned} \tag{1}$$

where  $L \in \mathbb{R}^{N \times N}$  is the linear, and  $h(\cdot) : \mathbb{R}^N \rightarrow \mathbb{R}^N$  the nonlinear, part of the system. We are mainly interested in dynamical systems whose solution could be effectively approximated on a manifold of lower dimension,  $\mathcal{V} \in \mathbb{R}^m \subset \mathbb{R}^N$  [e.g. 26]. Ideally, the dimension of this manifold is much smaller than that of the system, i.e.  $m \ll N$ . For the classic Galerkin-based reduced-order modeling, a linear decomposition of the form,

$$u(t) \approx \bar{u} + Va \tag{2}$$

is used, where  $\bar{u} \in \mathbb{R}^N$  is a reference value, the columns of  $V = [v_1, \dots, v_m] \in \mathbb{R}^{N \times m}$  a basis of the  $m$ -dimensional subspace  $\mathcal{V}$ , and  $a \in \mathbb{R}^m$  the vector of coefficients corresponding to the reduced basis. A popular choice for this basis is the proper-orthogonal-decomposition (POD) that defines the subspace such that the manifold  $\mathcal{V}$  preserves the variance of the system as much as possible when projected on  $V$  for a given  $m$ . The reference value ( $\bar{u}$ ) is then commonly chosen as the mean of the system state, in order to prevent the first reduced coefficient from containing the majority of the energy of the system and to help stabilize the reduced system [35].

Now, substituting Eq. 2 into Eq. 1, and projecting the result on the orthonormal modes  $V$ , we obtain the following set of ordinary differential equations for the coefficients  $a$ ,

$$\begin{aligned} \frac{da}{dt} &= V^T LVa + V^T h(\bar{u} + Va) + V^T L\bar{u} \\ a(0) &= V^T(u_0 - \bar{u}). \end{aligned} \tag{3}$$

This  $m$  dimensional system, with  $m \ll N$ , is computationally much cheaper than the original FOM Eq. 2. This method of dimensionality reduction is commonly referred to as the POD Galerkin Projection (POD-GP) method. It can suffer from a number of issues. First, the truncated modes can play an important role in the dynamical behaviour of the system, and neglecting them can thus lead to a very different forecast [44]. Second, the error in the reduced state may be simply too large for truncation, i.e. the POD reduction is not efficient. Third, if steady POD are employed, they may quickly become irrelevant for the evolving system state [82, 26, 27]. To address these issues, several methods try to represent the effect of the truncated modes. The most common approaches introduce a nonlinear parameterization of the coefficients [e.g. 56] in Eq. 3, however, they are not yet generally applicable to all classes of closures.

The geometric interpretation of the goal of closure modeling for ROMs is sketched in Fig. 1. The FOM solution of our dynamical system lies outside the lower dimension manifold,  $\mathcal{V}$ . A ROM approximate solution, denoted by  $u^{ROM}$ , starts with the projection of the full-order initial condition onto the manifold,  $VV^T u(0)$ , but quickly diverges from the actual projection of the full-order solution onto the manifold ( $VV^T u$ ), often leading to a significant source of error. A closure model in this case basically attempts to keep the updated ‘‘closed’’ solution,  $u^{ROM+C}$ , as close as possible to the actual projection of the FOM solution ( $VV^T u$ ) which can be seen as the truth.

## 2.2 Subgrid-Scale Processes

A key decision while setting up any numerical simulation is the selection of spatio-temporal resolution, which is in general limited by the computing power available. Using a coarse resolution (low-fidelity) model may however lead to a number of undesired artifacts, such as missing critical scales and processes for longer-term predictions or numerical diffusion that causes unintended or unacceptable results [96, 45]. These artifacts become especially important in the case of ocean models. For example, present-day global observing systems and global model solutions only resolve open-ocean mesoscale processes ( $\mathcal{O}(10 - 100km)$ ), but the submesoscale (subgrid-scale) processes do have global consequences, in relation to the mechanisms of

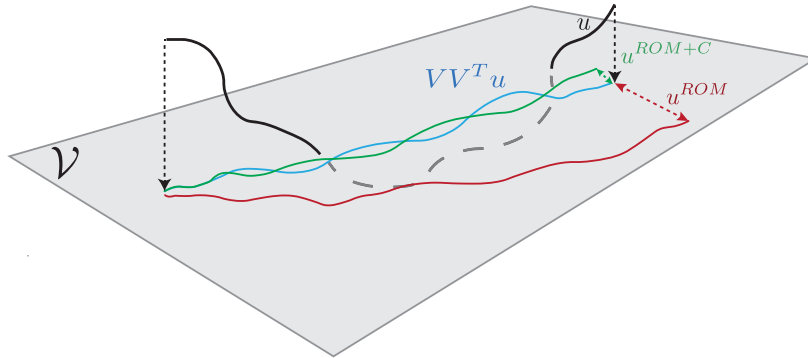


Figure 1: Geometric interpretation of the closure for reduced-order-models (ROMs).  $u$  (—): Solution to the full-order-model (FOM);  $VV^T u$  (—): Projection of  $u$  on the subspace  $V$ ;  $u^{ROM}$  (—): Solution to the proper-orthogonal-decomposition Galerkin-projection (POD-GP) ROM; and,  $u^{ROM+C}$  (—): Solution to POD-GP ROM with closure. Adapted from [90].

energy dissipation in the general circulation, vertical flux of material concentrations, and intermediate-scale horizontal dispersal of materials [60, 61, 20, 29]. The neglected and unresolved scales along with their interactions with the resolved ones are then at the core of closure parameterizations. Most present oceanic models consist of a nonlinear system of PDEs, each of a nonlinear advection type, supplemented by other possible diagnostic nonlinear equations, and boundary conditions. There is however no unique way of defining such parameterizations and multiple approaches such as non-dimensional analyses, physical balance hypotheses, statistical correlation constraints, and other empirical methods are commonly employed to develop closure models. Similar statements can be made for atmospheric, Earth system, and climate models [37, 83]. For all these applications, a general approach for subgrid-scale closures would thus be most useful.

### 2.3 Simplification of Complex Dynamical Systems

Due to incomplete understanding and limited measurements, it is common when modeling natural dynamical systems that the dynamics cannot be accurately explained just by using conservation laws and fundamental process equations. In such cases, the number of candidate models and equations can be almost as large as the number of modelers. The resulting models then also greatly vary in terms of their complexity. More complex models can capture key processes and feedbacks. Complexity is increased by adding more parameters and parameterizations to the existing components (state variables) of the dynamical model, but at some point, it quickly becomes inevitable to add and model new components to capture the underlying natural processes accurately, hence further increasing model complexity [64, 25, 59]. This is common, for example, in marine ecosystem models, where simpler models only resolve the broad biogeochemical classes, while more complex models capture detailed sub-classes [92, 53]. Increasing the number of components however can come at great computational cost, can increase the overall uncertainty, and can lead to loss of accuracy or stability due to the nonlinearities. Also, the unknown parameters for models with more components are calibrated from available data and the optimization process and parameter estimation quickly become challenging with the increase in complexity, due to the simultaneous explosion in the number of unknown parameters [74]. Thus, instead of adding more unknown parameterizations or increasing the number of components, one might use adaptive models [47, 46] and in general the present neural closure models to incorporate the effects of missing processes in low-complexity models, enabling them to adapt and emulate the response from high-complexity models.

### 3 Methodology

In this section, we develop the novel and versatile methodology for learning data-assisted closure models for dynamical systems. We first review the popular Mori-Zwanzig (MZ) formulation [85, 18, 33] which derives the exact functional form of the effects of truncated dynamics for common reduced models. Unfortunately, apart for very simple linear dynamical systems, the use of this formulation is very challenging without making unjustified approximations and simplifications. The MZ formulation, however, will inspire the methodological contributions of the present work.

#### 3.1 Mori-Zwanzig Formulation

Without loss of generality, the full nonlinear dynamical system model is written as,

$$\left. \begin{aligned} \frac{du_k(t)}{dt} &= R_k(u(t), t), \\ u_k(0) &= u_{0k} \end{aligned} \right\}, \quad k \in \mathfrak{F}. \quad (4)$$

The full state vector is  $u = (\{u_k\})$ ,  $k \in \mathfrak{F} = \mathfrak{R} \cup \mathfrak{U}$ , where  $\mathfrak{R}$  is the set corresponding to the resolved variables (e.g. coarse field or reduced variables), and  $\mathfrak{U}$  the set corresponding to the unresolved variables (e.g. subgrid field or complement variables), which as a union,  $\mathfrak{F}$ , form the set for full space of variables. We also denote  $u = \{\hat{u}, \tilde{u}\}$  where  $\hat{u} = (\{u_k\})$ ,  $k \in \mathfrak{R}$  and  $\tilde{u} = (\{u_k\})$ ,  $k \in \mathfrak{U}$ . Similarly,  $u_0 = \{\hat{u}_0, \tilde{u}_0\}$ , with  $\hat{u}_0 = (\{u_{0k}\})$ ,  $k \in \mathfrak{R}$  and  $\tilde{u}_0 = (\{u_{0k}\})$ ,  $k \in \mathfrak{U}$ .

We can write the above non-linear system of ODEs (Eq. 4) exactly as a system of linear PDEs by casting it in the Liouville form,

$$\left. \begin{aligned} \frac{\partial \phi_k}{\partial t} &= L\phi_k, \\ \phi_k(u_0, 0) &= u_{0k} \end{aligned} \right\}, \quad k \in \mathfrak{F}, \quad (5)$$

where the Liouville operator is  $L = \sum_{i \in \mathfrak{F}} R_i(u_0) \frac{\partial}{\partial u_{0i}}$ , with  $R_i$  denoting element  $i$  of the full model dynamics (Eq. 4). The solution of Eq. 5 is given by  $u_k(u_0, t) = \phi_k(u_0, t) = e^{tL} \phi_k(u_0, 0)$ . Hence, we can also rewrite Eq. 5 as,

$$\frac{\partial}{\partial t} e^{tL} u_{0k} = L e^{tL} u_{0k}, \quad k \in \mathfrak{F}. \quad (6)$$

Now, let  $P$  be a orthogonal projection on the space of functions of the resolved initial conditions  $\hat{u}_0$ , such that, for any nonlinear function  $h(u_0) = h(\{\hat{u}_0, \tilde{u}_0\})$ , then  $P(h(u_0)) = h(\hat{u}_0)$ . Similarly,  $Q = I - P$  is the projection on the null space of  $P$ . It is important to note that the projectors  $P$  and  $Q$  used in this formulation are fundamentally different from L2 projectors. Using the Dyson's formula  $e^{tL} = e^{tQL} + \int_0^t e^{(t-s)L} P L e^{sQL} ds$ , and noting that  $L$  and  $e^{tL}$  commute, we can then exactly rewrite Eq. 6 as,

$$\frac{\partial}{\partial t} e^{tL} u_{0k} = e^{tL} P L u_{0k} + e^{tQL} Q L u_{0k} + \int_0^t e^{(t-s)L} P L e^{sQL} Q L u_{0k} ds, \quad k \in \mathfrak{R}, \quad (7)$$

which is called the Mori-Zwanzig (MZ) formulation. Importantly, the above equation is an exact representation of Eq. 6 for the resolved components. For convenience, we denote  $F_k(u_0, t) = e^{tQL} Q L u_{0k}$  and  $K_k(u_0, t) = P L F_k(u_0, t)$ , and thus further rewrite Eq. 7 as,

$$\frac{\partial}{\partial t} u_k(u_0, t) = \underbrace{R_k(\hat{u}(u_0, t))}_{\text{Markovian}} + \underbrace{F_k(u_0, t)}_{\text{Noise}} + \underbrace{\int_0^t K_k(\hat{u}(u_0, t-s), s) ds}_{\text{Memory}}, \quad k \in \mathfrak{R}, \quad (8)$$

where  $R_k$  is again the same as that in the full model dynamics given by Eq. 4. Eq. 8 provides useful guidance for closure modeling. The first term in Eq. 8 is the Markovian term dependent only on the values of the variables at the present time, while the closure consists of two terms: the noise term and a memory term that is non-Markovian. We can further simplify Eq. 8 by applying the  $P$  projection and using the fact that

the noise term lives in the null space of  $P$  for all times, which could be easily proved. For ROMs with initial conditions devoid of any unresolved dynamics, i.e.  $\tilde{u}_0 = 0$  and thus  $u_0 = \hat{u}_0$ , we then retain the exact dynamics after the projection step, noticing in this case that  $Pu_k(u_0, t) = u_k(\hat{u}_0, t), \forall k \in \mathfrak{R}$ ,

$$\frac{\partial}{\partial t} u_k(\hat{u}_0, t) = PR_k(\hat{u}(\hat{u}_0, t)) + P \int_0^t K_k(\hat{u}(\hat{u}_0, t-s), s) ds, \quad k \in \mathfrak{R}. \quad (9)$$

Hence, for such systems, the closure model would only consider the non-Markovian memory term. The above derivation of the MZ formulation has been adapted from [85, 90, 33].

The MZ formulation clearly shows that a non-Markovian closure term requiring time-lagged state information is theoretically needed to model the missing dynamics. This theoretical basis however seems to be mainly related to the first two classes of low-fidelity dynamical systems (Sec. 2), ROMs and coarse resolution models. This is because the third category of dynamical models often represents complex biological systems that are commonly studied using ODEs, with one state variable per biological component. Such ODEs implicitly assume that information between state variables is exchanged instantaneously. In reality, however, there is often a time-delay for several reasons. First, changes in populations or reactions have non-negligible time-scales [e.g. 41, 22]. Such time-scales are introduced in more complex models by modeling intermediate biological states. Hence, the time response of lower-complexity models can be comparable to that of high-complexity models only by explicitly introducing delays [41, 8, 32, 87]. Second, many reactive systems are modeled assuming smooth concentration fields of state variables governed by PDEs with fluid flow advection and/or mixing, leading to advection-diffusion-reaction PDEs [36, 24]. In that case, simplified models still require time-delays due to the neglected reactive or biogeochemical dynamics but now also due to truncated modes and/or subgrid-scale processes of numerical models. For all of these reasons, the need for memory based closure terms in the simplification of complex dynamical systems is clearly justified.

There are some results for data-assisted / data-driven closure modeling based on the MZ formulation. Some schemes create a coupled system of stochastic differential equation using appropriate hidden-variables for approximate Markovization of the non-Markovian term [40, 9]. Others use a variational approach to derive nonlinear parameterizations approximating the Markovian term [15]. Schemes using machine learning could be much more versatile but results so far [90, 89] lack the rigorous use of the theory for time-delay systems [73].

### 3.2 Neural Delay Differential Equations

The non-Markovian closure terms with time-lagged state information lead us to the use of delay differential equations (DDEs) [23]. DDEs have been widely used in many fields such as biology [84, 54], pharmacokinetic-pharmacodynamics [39], chemistry [78], economics [38], transportation [55], control theory [43], climate dynamics [30, 6], etc. Next, we summarize the state of the art for learning and solving differential equations using neural-networks (NNs) and develop theory and schemes for neural DDEs including adjoint equations for backpropagation.

The interpretation of residual networks as time integration schemes and flow maps for dynamical systems has led to pioneering development of neural ordinary differential equations (nODEs) [16]. A nODE parameterizes an ODE using a neural-network and solves the initial value problem (IVP) given by,

$$\begin{aligned} \frac{du(t)}{dt} &= f_{NN}(u(t), t; \theta), & t \in (0, T] \\ u(0) &= u_o, \end{aligned} \quad (10)$$

where  $f_{NN}$  is the prescribed neural-network and  $\theta$  are the weights. Starting from the initial conditions, the nODE (Eq. 10) is integrated forward in time using any time-integration scheme, and then gradients are computed based on a loss function using the adjoint sensitivity method. The gradient computation boils down to solving a second ODE backwards in time. Using standard backpropagation for Eq. 10 has however several issues: it would be very memory expensive as one needs to store the state at every time step; its computational cost would increase when using higher-order time-integration or *implicit* schemes; and, it might become infeasible if the forward time-integration code does not support automatic differentiation. The adjoint method, however, provides a backpropagation for nODEs [16] that is memory efficient and flexible

as it treats the time-integration scheme as a “black-box”. In our case, we need to incorporate state-delays. Though extending the nODE framework to incorporate DDEs comes under the ambit of universal differential equations (UDEs) [70], deeper investigations are warranted. First, the UDEs are presently implemented using the Julia library DiffEqFlux.jl [69] which can perform automatic adjoint equation solves, but other popular open-source languages such as Python and R, and ML-Frameworks such as TensorFlow [1], PyTorch [65], etc., would require explicit derivation and coding of the corresponding adjoint equations. Second, we need to study two different types of DDEs, the discrete and distributed delays, which it turns out require very different architectures. Next, we thus develop the theory and schemes for efficient implementation of neural delay differential equations (nDDEs) in any programming language.

### 3.2.1 Discrete Delays

The most popular form of delay differential equations (DDEs) is,

$$\begin{aligned} \frac{du(t)}{dt} &= f(u(t), u(t - \tau_1), \dots, u(t - \tau_K), t), \quad t \in (0, T] \\ u(t) &= h(t), \quad t \leq 0 \end{aligned} \quad (11)$$

where  $\tau_1, \dots, \tau_K$  are  $K$  number of discrete-delays (discrete DDEs). Instead of a single initial value as in the case of ODEs, DDEs require specification of a history function,  $h(t)$ . Due to the presence of a given fixed number delays, we can parameterize the above system by replacing the time-derivative function with potentially any type of NNs. For example, to use fully-connected NNs we would concatenate all the delayed states vertically to form the input vector, or concatenate them horizontally to form an input matrix for a convolutional NN. However, recurrent NN (RNN) architectures, such as simple-RNNs, LSTMs, GRUs, etc., are ideal and most efficient for our need due to the time-series nature of the delayed states. We can assume that the discrete delays are evenly spaced (this is not a hard requirement as we can easily extend schemes to irregularly spaced discrete-delays using ODE-RNNs [79], but for brevity we make this assumption) and use a RNN with weights  $\theta$ . Hence, our new discrete-DDE system can be written as,

$$\begin{aligned} \frac{du(t)}{dt} &= f_{RNN}(u(t), u(t - \tau_1), \dots, u(t - \tau_K), t; \theta), \quad t \in (0, T] \\ u(t) &= h(t), \quad t \leq 0, \end{aligned} \quad (12)$$

where  $f_{RNN}(\bullet; \theta)$  is the recurrent architecture. We refer to this parameterization of discrete DDEs as *discrete-nDDE*. The graphical representation of Eq. 12 in time-discretized form is depicted in Figure 2a. Let data be available at  $M$  times,  $T_1 < \dots < T_M \leq T$ . We then optimize the scalar loss function given by,  $\mathcal{L} = \int_0^T \sum_{i=1}^M l(u(t)) \delta(t - T_i) dt$ , where  $\delta(t)$  is the Kronecker delta function. In order to use any gradient descent algorithm to perform this optimization, we require gradient of the loss function w.r.t. the weights of the RNN,  $\theta$ . Using the adjoint sensitivity method [13] to compute the required gradients, we start by writing the Lagrangian for the above system,

$$\begin{aligned} L = \mathcal{L}(u(t)) &+ \int_0^T \lambda^T(t) (d_t u(t) - f_{RNN}(u(t), u(t - \tau_1), \dots, u(t - \tau_K), t; \theta)) dt \\ &+ \int_{-\tau_K}^0 \mu^T(t) (u(t) - h(t)) dt, \end{aligned} \quad (13)$$

where  $\lambda(t)$  and  $\mu(t)$  are the Lagrangian variables. In order to find the gradients of  $L$  w.r.t.  $\theta$ , we first solve the following adjoint equation (for brevity we denote,  $\frac{\partial}{\partial(\bullet)} \equiv \partial(\bullet)$  and  $\frac{d}{d(\bullet)} \equiv d(\bullet)$ ),

$$\begin{aligned} d_t \lambda^T(t) &= \sum_{i=1}^M \partial_{u(t)} l(u(t)) \delta(t - T_i) - \lambda^T(t) \partial_{u(t)} f_{RNN}(\bullet, t; \theta) \\ &- \sum_{i=1}^K \lambda^T(t + \tau_i) \partial_{u(t - \tau_i)} f_{RNN}(\bullet, t + \tau_i; \theta), \quad t \in [0, T] \\ \lambda(t) &= 0, \quad t \geq T. \end{aligned} \quad (14)$$

Details of the derivation of the above adjoint Eq. 14 are in the accompanying *Supplementary Information*. Note that Eq. 14 needs to be solved backward in time, and one would require access to  $u(t)$ ,  $0 \leq t \leq T$ . In the original nODE work [16], Eq. 12 is solved backward in time and augmented with the adjoint Eq. 14, so as to shrink the memory footprint by avoiding the need to save  $u$  at every time-step. Solving Eq. 12 backward can however lead to catastrophic numerical instabilities as is well known in data assimilation [94, 75]. Improvements have been proposed, such as the ANODE method [31], but they are not applicable in case of DDEs. In our present implementation, in order to access  $u(t)$ ,  $0 \leq t \leq T$ , while solving the adjoint equation, we create and continuously update an interpolation function using the  $u$  obtained at every time-step as we solve Eq. 12 forward in time. To be more memory efficient, we can, for example, use the interpolated reverse dynamic method (IRDM) [21], which would involve only storing  $u$  at Chebyshev time points to perform a barycentric Lagrange interpolation later. After solving for  $\lambda$ , we can compute the required gradients as,

$$d_{\theta}L = - \int_0^T \lambda^T(t) \partial_{\theta} f_{RNN}(\bullet, t; \theta) dt. \quad (15)$$

Finally, using any gradient descent algorithm, we can find the optimal values of the weights  $\theta$ .

### 3.2.2 Distributed Delays

In some applications, the delay is distributed over some past time-period [72],

$$\begin{aligned} \frac{du(t)}{dt} &= f\left(u(t), \int_{t-\tau_2}^{t-\tau_1} g(u(\tau)) d\tau, t\right), \quad t \in (0, T] \\ u(t) &= h(t), \quad t \leq 0. \end{aligned} \quad (16)$$

It should be noted that the discrete DDEs can be written as a special case of distributed DDEs using dirac-delta functions. We can approximate the two functions  $f$  and  $g$  using two different neural-networks, and re-write the above Eqs. 16 as our new coupled discrete DDEs,

$$\begin{aligned} \frac{du(t)}{dt} &= f_{NN}(u(t), y(t), t; \theta), \quad t \in (0, T] \\ \frac{dy(t)}{dt} &= g_{NN}(u(t - \tau_1); \phi) - g_{NN}(u(t - \tau_2); \phi), \quad t \in (0, T] \\ u(t) &= h(t), \quad \tau_2 \leq t \leq 0 \\ y(0) &= \int_{-\tau_2}^{-\tau_1} g_{NN}(h(t)) dt \end{aligned} \quad (17)$$

where  $f_{NN}(\bullet, t; \theta)$  and  $g_{NN}(\bullet; \phi)$  are the two NNs parameterized by  $\theta$  and  $\phi$  respectively. We refer to this parameterization of distributed DDEs as *distributed-nDDE*. The graphical representation of the above system (Eqs. 17) in time-discretized form is depicted in Figure 2b. It is interesting to note that in the case of distributed-delays, we end up with a completely different architecture (as compared to discrete-nDDE) consisting of two coupled NNs. We can consider  $f_{NN}$  as the main network, and  $g_{NN}$  as the auxiliary network. Again, we define a scalar loss function given by  $\mathcal{L} = \int_0^T \sum_{i=1}^M l(u(t)) \delta(t - T_i) dt$  for the available data at  $M$  times,  $T_1 < \dots < T_M \leq T$ . The Lagrangian for the above system is,

$$\begin{aligned} L &= \mathcal{L}(u(t)) + \int_0^T \lambda^T(t) (d_t u(t) - f_{NN}(u(t), y(t), t; \theta)) dt \\ &+ \int_0^T \mu^T(t) (d_t y(t) - g_{NN}(u(t - \tau_1); \phi) + g_{NN}(u(t - \tau_2); \phi)) dt \\ &+ \int_{-\tau_2}^0 \gamma^T(t) (u(t) - h(t)) dt + \alpha^T \left( y(0) - \int_{-\tau_2}^{-\tau_1} g_{NN}(h(t)) dt \right), \end{aligned} \quad (18)$$

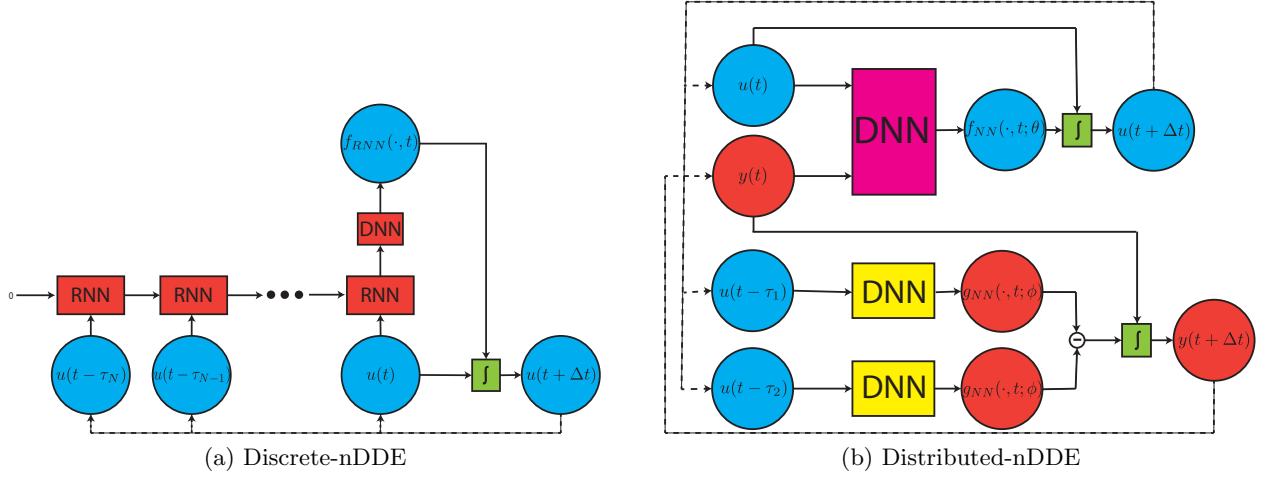


Figure 2: Graphical representation of the time discretized neural delay differential equations (nDDEs). The blocks labeled *RNN* and *DNN* represent any recurrent or deep neural-network architectures respectively. The block labeled  $\int$  symbolizes any time-integration scheme.

where  $\lambda(t)$ ,  $\mu(t)$ ,  $\gamma(t)$ , and  $\alpha$  are the Lagrangian variables. In order to find the gradients of  $L$  w.r.t. the parameters of the two NNs, we first solve the following coupled adjoint equations backward in time,

$$\begin{aligned}
d_t \lambda^T(t) &= \sum_{i=1}^M \partial_{u(t)} l(u(t)) \delta(t - T_i) - \lambda^T(t) \partial_{u(t)} f_{NN}(\bullet, t; \theta) \\
&\quad - \mu^T(t + \tau_1) \partial_{u(t - \tau_1)} g_{NN}(\bullet, t + \tau_1; \phi) \\
&\quad + \mu^T(t + \tau_2) \partial_{u(t - \tau_2)} g_{NN}(\bullet, t + \tau_2; \phi), \quad t \in [0, T] \\
d_t \mu^T(t) &= -\lambda^T(t) \partial_{y(t)} f_{NN}(\bullet, t; \theta), \quad t \in [0, T] \\
\lambda(t) &= 0, \quad \text{and} \quad \mu(t) = 0, \quad t \geq T.
\end{aligned} \tag{19}$$

Details of the derivation of the above adjoint Eq. 19 are in the accompanying *Supplementary Information*. For accessing  $u$  values while solving the adjoint equations, we use the same approach as that mentioned for discrete-nDDE (Sec. 3.2.1). After solving for  $\lambda$  and  $\mu$ , we can compute the required gradients as,

$$\begin{aligned}
d_\theta \mathcal{L} &= - \int_0^T \lambda^T(t) \partial_\theta f_{NN}(\bullet, t; \theta) dt \\
d_\phi \mathcal{L} &= - \int_0^T \mu^T(t) \partial_\phi g_{NN}(\bullet, t; \phi) dt.
\end{aligned} \tag{20}$$

Finally, using any gradient descent algorithm, we can optimize the neural-networks  $f_{NN}$  and  $g_{NN}$ , and find the optimal values of the weights  $\theta$  and  $\phi$ .

### 3.3 Neural Closure Models

Now that we have the framework for representing delay differential equations using neural-networks, we can replace the non-Markovian memory term in Eq. 9 using nDDEs to obtain a hybrid closure model which could be trained using data from high-fidelity simulations. The modified low-fidelity dynamical system with the nDDE closures, which approximates the high-fidelity model would be given by,

$$\begin{aligned}
\frac{\partial \hat{u}(t)}{\partial t} &= \underbrace{PR(\hat{u}(t))}_{\text{Low-Fidelity}} + \underbrace{f_{RNN}(\hat{u}(t), \hat{u}(t - \tau_1), \dots, \hat{u}(t - \tau_K), t; \theta)}_{\text{Neural Closure}} \\
\hat{u}(0) &= \hat{u}_0, \quad t \leq 0
\end{aligned} \tag{21}$$

using discrete-delays, or by,

$$\frac{\partial \hat{u}(t)}{\partial t} = \underbrace{PR(\hat{u}(t))}_{\text{Low-Fidelity}} + \underbrace{f_{NN}\left(\hat{u}(t), \int_{t-\tau_2}^{t-\tau_1} g_{NN}(\hat{u}(\tau); \phi) d\tau, t; \theta\right)}_{\text{Neural Closure}} \quad (22)$$

$$\hat{u}(0) = \hat{u}_0, \quad t \leq 0$$

using distributed-delays. The initial conditions at  $t = 0$ ,  $\hat{u}_0$ , can be used for  $t < 0$  as well, as an approximation. Apart from the neural-network architectures, the amount of delay to be used also becomes a hyperparameter to tune. These novel *neural closure models* provides extreme flexibility in designing the non-Markovian memory term in order to incorporate subject matter expert insights. At the same time, we can also learn the unknown parts of the Markovian low-fidelity model using nODEs if the need arises. Next, we will compare the performance and advantages of using no-delays (nODEs), discrete-delays (discrete-nDDEs), and distributed-delays (distributed-nDDEs) in closure terms for various low-fidelity dynamical systems.

## 4 Result and Discussion

After presenting the main classes of low-fidelity dynamical models that require closure (Sec. 2), we developed a novel, versatile, and rigorous methodology for learning and modeling non-Markovian closure terms using nDDEs (Sec. 3). The resulting neural closure models have their theoretical underpinning in the Mori-Zwanzig formulation and in the presence of inherent delays in models of complex natural dynamical systems such as biogeochemical systems. Now, we evaluate the performance and advantages of these new neural closure models over those of neural ODEs (Markovian).

We run experiments for each of the three classes of low-fidelity models requiring closures (Sec. 2). For each experiment, we follow the same training protocol for nODEs (no-delays) and the two nDDEs, discrete-nDDE (discrete-delays) and distributed-nDDE (distributed-delays), closure models. The training data are regularly sampled from high-fidelity simulations in all experiments, but this is not a requirement. For evaluation, we compare the performance for the training period (period for which high-fidelity data snapshots are used for training) but also for longer-term predictions well past this period. As the field of scientific machine learning (SciML; [71]) is relatively new, the metrics for performance evaluation vary greatly. On the one hand, many learning studies randomly sample small time-sequences from a given period for which high-fidelity data are available, and then split them into training, validation, and test sets [58]. Because the training and test sets belong to the same time-domain, predicting the unseen data is then easy for the learned network. On the other hand, for the few studies where the training and test (prediction) periods do not overlap, the prediction period is often much shorter than the training period [97]. In the present work, we consider a more stringent evaluation: the prediction period is at least of the same length as the training period and has no overlap with it. Of course, other evaluation metrics are possible and there is indeed a need for standardization of evaluation procedures in the SciML community.

### 4.1 Experiments 1: Advecting Shock - Reduced Order Model

For the first experiments, neural closure models learn the closure of proper-orthogonal-decomposition Galerkin projection (POD-GP) based reduced order model of the advecting shock problem. The full-order-model (FOM) for this problem is given by the Burger’s equation,

$$\frac{\partial u}{\partial t} + u \frac{\partial u}{\partial x} = \nu \frac{\partial^2 u}{\partial x^2} \quad (23)$$

where  $\nu$  is the non-dimensional diffusion coefficient. The initial and boundary conditions are

$$u(x, 0) = \frac{x}{1 + \sqrt{\frac{1}{t_0}} \exp\left(Re \frac{x^2}{4}\right)}, \quad (24)$$

$$u(0, t) = 0, \quad \text{and} \quad u(L, t) = 0,$$

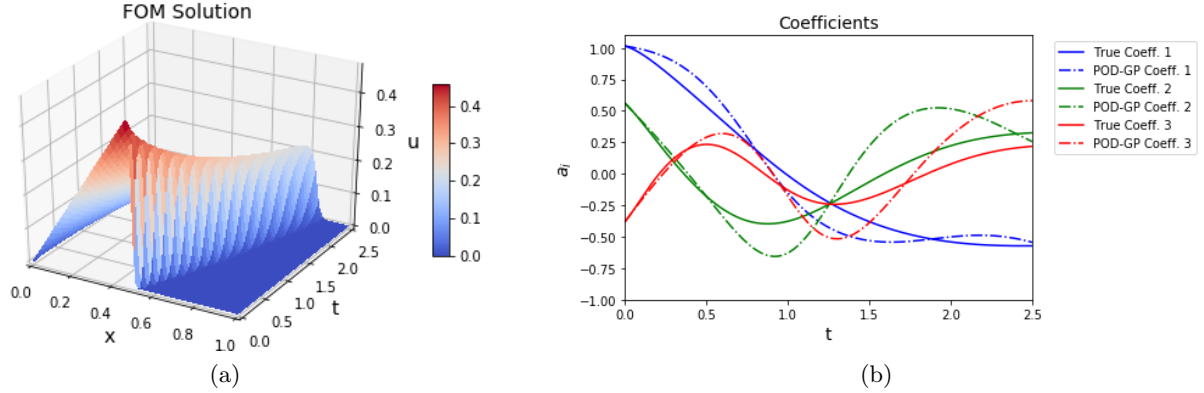


Figure 3: (a) Solution of the full-order-model (FOM) (Eqs. 23 and 24) for domain length  $L = 1$ , maximum time  $T = 2.5$ , and Reynolds number  $Re = 1000$ , plotted in a Hovmöller diagram. (b) Comparison of the coefficients of the proper-orthogonal-decomposition Galerkin-projection (POD-GP) reduced-order-model (ROM; Eq. 25) of the first three modes (*dashed-dot*) with the true coefficients (*solid*), i.e. the solution of the FOM for initial conditions composed only of the resolved modes (first three) and projected onto the same.

where  $Re = 1/\nu$  and  $t_0 = \exp(Re/8)$ . Let the POD of the state variable  $u(x, t)$  be given by,  $u(x, t) = \bar{u}(x) + \sum_{i=1}^m u_i(x)a_i(t)$ , we obtain the reduced-order equations as outlined in Section 22.1,

$$\begin{aligned} \frac{da_k}{dt} = & - \left\langle \bar{u} \frac{\partial \bar{u}}{\partial t}, u_k \right\rangle - a_i \left\langle u_i \frac{\partial \bar{u}}{\partial t}, u_k \right\rangle - a_j \left\langle \bar{u} \frac{\partial u_j}{\partial t}, u_k \right\rangle \\ & - a_i a_j \left\langle u_i \frac{\partial u_j}{\partial t}, u_k \right\rangle + \left\langle \nu \frac{\partial^2 \bar{u}}{\partial x^2}, u_k \right\rangle + a_i \left\langle \nu \frac{\partial^2 u_i}{\partial x^2}, u_k \right\rangle, \end{aligned} \quad (25)$$

$$a_k(0) = \langle (u(x, 0) - \bar{u}(x)), u_k(x) \rangle.$$

The solution of the FOM (Eqs. 23 and 24) for  $Re = 1000$ ,  $L = 1$ , and maximum time  $T = 2.5$ , is shown in Figure 3. The singular value decomposition (SVD) of this solution form the POD modes for the ROM. We only keep the first three modes which capture 66.2% of energy, thus requiring a closure. The evolution of the coefficients corresponding to the first three modes according to Eq. 25, is shown in Figure 3b. The high-fidelity or true coefficients are obtained solving the FOM (Eq. 23) with initial conditions without the contribution from the unresolved modes, i.e.  $u(x, 0) = \bar{u}(x) + \sum_{i=1}^3 u_i(x)a_i(0)$ , and projecting the obtained solution onto the first three modes. For comparison, we also present the true coefficients in Figure 3b, which is what the ROMs with neural closure are trying to match. For this true data generation, we solve the FOM with a time step of  $\Delta t = 0.01$ , and grid spacing of  $\Delta x = 0.01$ , using finite-difference schemes (upwind for the advection and central difference for the diffusion term) and an explicit Runge-Kutta (RK) time-integration of order (4)5 due to Dormand & Prince (*dopri5*; [34]).

For training our neural closure models for the advecting shock ROM (Eq. 25) with three modes, we only use the true coefficient values up to time  $t = 1.25$ . For testing, we make a prediction from  $t = 1.25$  to the maximum time  $T = 2.5$ . Thus, the training period is from  $t = 0$  to 1.25 and prediction period from  $t = 1.25$  to 2.5. We compare the three different closures: nODE (no-delays), discrete-nDDE, and distributed-nDDE with architecture details presented in Table 1. The architectures are of course not exactly the same for the three cases, but they are set-up to be of comparable expressive power. Mostly, we employ a bigger architecture for the no-delays case in order to help it compensate the lack of past information. We also ensure that the networks are neither under-parameterized nor over-parameterized. Along with the classical hyperparameters such as batch size, number of iterations per epoch, number of epochs, learning rate schedule, etc., we also have the delay values ( $\tau_1, \dots, \tau_K$  for discrete-nDDE; and  $\tau_1, \tau_2$  for distributed-nDDE) as additional hyperparameters to tune. We chose to only use two discrete delays for the discrete-nDDE in the present experiments. For training, we randomly select short time-sequences spanning only 6 time-steps and extract data at every other time-step to form batches of size 2. Each epoch consists of 12 iterations: this is calculated by dividing the number of time-steps in the training period by batch-size multiplied the

Category	Architecture	Act.	Delays	Trainable Parameters	
nODE (No-Delays)	$f_{NN}$		None	158	
	Input layer with 3 neurons	none			
	5 FC hidden layer with 5 neurons	tanh			
	FC output layer with 3 neurons	linear			
Discrete-nDDE	$f_{RNN}$		$\tau_1 = 0.075,$ $\tau_2 = 0.15$	63	
	Input layer with 3 neurons	none			
	Simple RNN layer with 5 neurons	tanh			
	FC output layer with 3 neurons	linear			
Distributed-nDDE	$f_{NN}$		$\tau_1 = 0,$ $\tau_2 = 0.175$	110	
	Input layer with 5 neurons	none			
	2 FC hidden layer with 5 neurons	tanh			
	FC output layer with 3 neurons	linear			
	$g_{NN}$				
	Input layer with 3 neurons	none			
	2 FC hidden layer with 3 neurons	tanh			
	FC output layer with 2 neurons	linear			

Table 1: Architectures for different neural closure models used in Experiments-1. FC stands for fully-connected and the last column notes the number of trainable parameters available.

length of short time-sequences, adding 1, and rounding up to the next integer. Further, we use the *RMSprop* optimizer with an exponentially decaying learning rate (LR) schedule (initial LR of 0.075, decay rate of 0.97, and 12 decay steps). For evaluation, at each epoch, we evolve the coefficient of the learned system using the RK time-integration scheme mentioned earlier, and compare them with the true coefficients using the time-averaged  $L_2$  error, which is also our loss function for training. The error for the time period  $t = 0$  to 1.25 forms the training loss, while the error for the time period  $t = 1.25$  to 2.5 forms the prediction loss.

The performance of the three neural closure models after 200 epochs (the stochastic gradient descent nearly converges, as evident from Figure 5) is evaluated by comparison with the true coefficients and with the POD-GP coefficients spanning both the training and prediction periods. Results are shown in Figure 4. The details of the architectures used to produce these results are given in Table 1. In three cases, we find that using no-delays (nODE), discrete-delays (discrete-nDDE), and distributed-delays (distributed-nDDE) perform equally well for the training period, exactly matching the true coefficients. As soon as one enters the prediction period, the nODE closure however quickly starts to diverge from the true coefficients, while both the discrete-nDDE and distributed-nDDE closures remain close to the true coefficients, only starting to slightly diverge in the second-half of the prediction period, but still maintaining a great improvement over just using the POD-GP model. The nDDE closures maintain a better performance than the nODE closure, even though the latter had a deeper architecture with significantly more trainable parameters. We also find that the performance of distributed-nDDE closure is a little worse than that of the discrete-nDDE closure for the later half of the prediction period. These observations are also corroborated from the time-averaged  $L_2$  losses, for both training and prediction periods with training epochs (Fig. 5). Due to the highly nonlinear nature of neural networks, analytical stability analyses are not direct. Nonetheless, we provide empirical stability results by extending the prediction period up to  $T = 6.25$  and reporting the root-mean-square-error (RMSE) as it evolves with time (Fig. 4). We find that both discrete-nDDE and distributed-nDDE closures, due to the existence of delays, may have a stronger dissipative character and thus show much better stability at later times than POD-GP and the nODE closure.

One might expect the distributed-delay (distributed-nDDE) to always perform better than the discrete-nDDE closure because of the presence of the integral of the state variable over a delay period instead of the state variable at specific points in the past. The former thus seemingly contains more information, but there is in fact no guarantee for this being true in all cases. We can derive an intuition for this from information theory. According to the data processing inequality [19], let  $X$  and  $Y$  be two random variables, then,

$$I(g(X); Y) \leq I(X; Y), \quad (26)$$

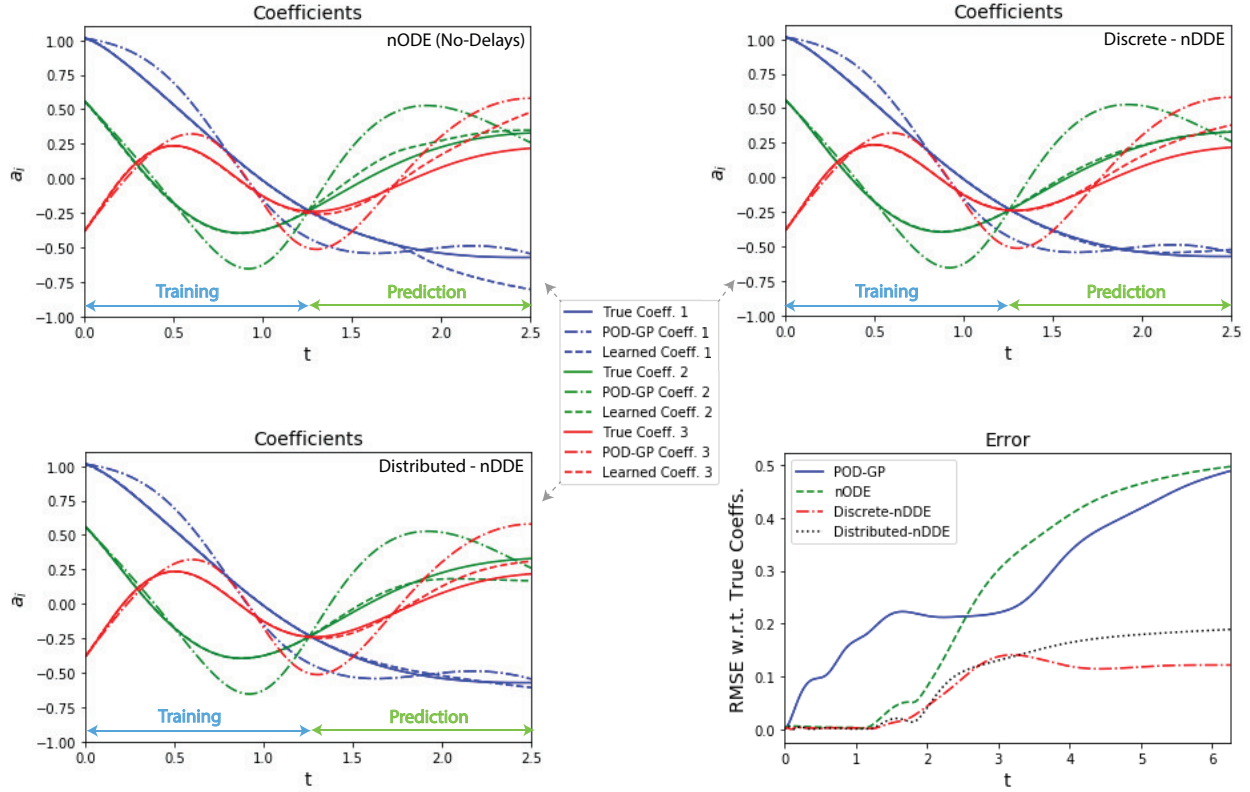


Figure 4: Comparison of the true coefficients (*solid*) with the coefficients from the POD-GP ROM (*dashed-dot*) and from the learned POD-GP ROM augmented with the three different neural closure models at the end of training (*dashed*). For each neural closure, the training period is from  $t = 0$  to 1.25 while the prediction period is from  $t = 1.25$  to 2.5. *Top-left*: neural ODEs with no-delays (nODE); *Top-right*: neural DDEs with discrete-delays (Discrete-nDDE); *Bottom-left*: neural DDEs with distributed-delays (Distributed-nDDE). *Bottom-right*: Evolution of root-mean-squared-error (RMSE) of coefficients from the four different ROMs for an extended prediction period up to  $T = 6.25$ . These results correspond to the architectures detailed in Table 1.

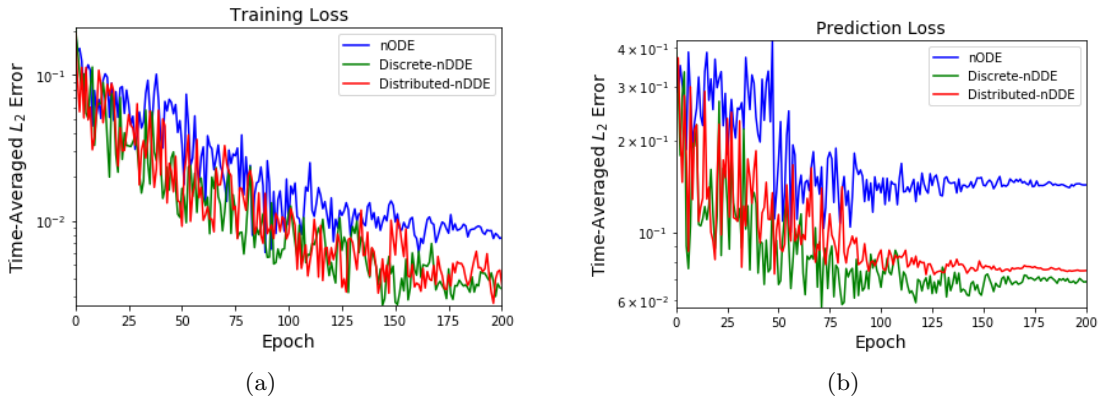


Figure 5: Variation with epochs of (a): training; and (b): prediction time-averaged  $L_2$  loss for the three neural closure models, while training for Experiments-1. These results accompany Figure 4 and the architectures detailed in Table 1.

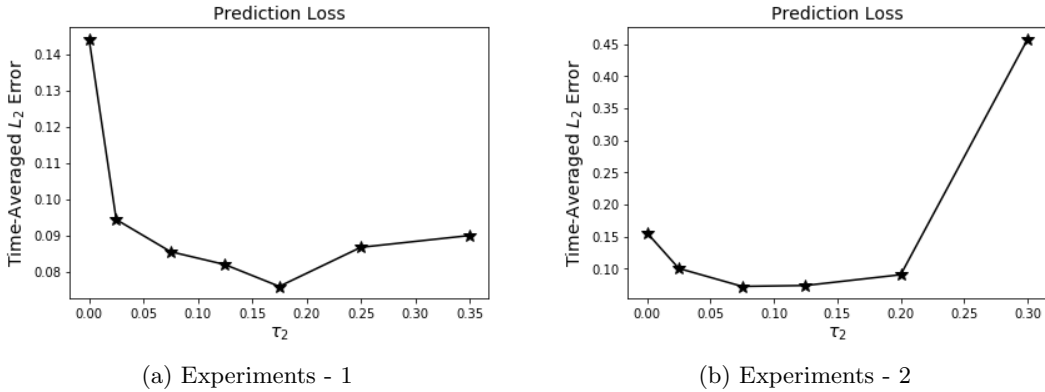


Figure 6: Variation of distributed-nDDE closure prediction loss (time-averaged  $L_2$  error) averaged over the last 50 and 30 training epoch for Experiments- 1 & 2, respectively. All the experiments have  $\tau_1 = 0$ , and different  $\tau_2$  (horizontal-axis). Note that  $\tau_2 = 0$  corresponds to the nODE closure.

where  $I$  is the mutual information and  $g$  is any function which post-processes  $X$ . Now, if  $X$  is composed of  $K$  random variables,  $X = \{X_1, \dots, X_K\}$ , and  $g(X) = X_1 + \dots + X_K$ , then,

$$I(X_1 + \dots + X_K; Y) \leq I(\{X_1, \dots, X_K\}; Y). \quad (27)$$

If we consider the effect of the integral of the state variable over the delay period in the case of distributed-nDDE as a data processing step, this might actually be decreasing the information content as compared to the discrete-nDDE closure. We use “might”, even though Eq. 27 is a strong bound, because in the present experiments we only use two delay values for the discrete-nDDE, while the integral in the distributed-nDDE is computed using many past state values, and also the architectures are different. Hence, a direct comparison using the data processing inequality (Eq. 27) is not possible, but it provides us with a plausible explanation.

We now study the effect of changing the amount of past information incorporated in the closure model on the time-averaged  $L_2$  error. For this, we fix  $\tau_1 = 0$  for the distributed-nDDE closure, and vary the values of only  $\tau_2$ , keeping the architecture the same (Table 1). First, for the training period, all closures once trained very closely matched the true coefficients. For the corresponding time-averaged training loss (not shown), we found no discernible trend and differences were mostly due the stochastic gradient descent. Second, for the prediction period, Fig. 6a shows the average prediction losses (time-averaged  $L_2$  error) between the last epochs 150 to 200, for different delay-period lengths. Results indicate that the average prediction loss first decreases and then increases as we incorporate more-and-more past information, starting from a very small delay period. For a specified architecture, neither too little nor too much past information is helpful: there is likely an optimal amount of information to incorporate. The initial improvement in the performance of the closure models as the delay period is increased is due to the increase in information content about what happened in the recent past. However, a particular network architecture of finite size will have a limit on capturing the increasing information content effectively due to its limited expressive power, thus leading to a decrease in performance when too much information is provided. Some studies in the existing literature attempt to derive analytical expressions for the optimal memory length, making many approximations in the process [52]. If such estimates of optimal memory length were derivable for the present nDDEs, then they can be used to determine the optimal network architecture required for a given dynamical system. Another option is to learn the delay amount as a part of the training process itself, however, this requires re-derivation of the adjoint equations.

In addition to the results just illustrated, we completed many other experiments-1 to assess the sensitivity of our framework to various parameters. In all cases, the time-period corresponding to the training data should be at least equal to one characteristic time-scale of the dynamics, otherwise the prediction performance deteriorated. Adding the neural closure to the low-fidelity model improved its matching with the high-fidelity data in nearly all cases. Its performance deteriorated with increasing the length of the time-sequences used to form the batches, and also with increasing the batch-size (the number of iterations per epoch is a dependent

hyperparameter as mentioned earlier). This also led to an increase in training time. Using an exponentially decaying learning schedule over a constant learning rate tremendously improved learning performance and reduced the number of epochs needed. Further, training times increased when using more delay times in the case of discrete-nDDE, or when using LSTMs over simple-RNNs. In general, we also found that the training time for discrete-nDDEs was nearly double that for distributed-nDDEs. Such behaviors by machine learning methods are difficult to anticipate in advance but they should be mentioned.

Overall, in the experiments-1, we find that using memory-based neural closure models as we derived from the Mori-Zwanzig formulation is advantageous over just a Markovian closure. Using the new nDDEs as closure models helps maintain generalizability of the learned models for longer time-periods, and significantly reduces the longer-term prediction error of the ROM.

## 4.2 Experiments 2: Advecting Shock - Subgrid-Scale Processes

In the second experiments, we again use the advecting shock problem governed by the Burger’s equation (Eq. 23), but we now reduce the computational cost of the FOM by coarsening the spatial resolution, again leading to the need of a closure model (Sec. 2.2). For the high-fidelity/high-resolution solution, we employ a fine grid with the number of grid point in the  $x$  direction  $N_x = 100$ , while for the low-fidelity/low-resolution solution, we employ a 4 times coarser grid with  $N_x = 25$ . A comparison of high- and low- resolution solutions solved using exactly the same numerical schemes and time-step of  $\Delta t = 0.01$  is provided in Fig. 7. We observe that by decreasing the resolution, we introduce numerical diffusion and error in the location of the shock peak at later times. The goal of the neural closure models in these experiments is thus to augment the low-resolution model such that it matches the sub-sampled/interpolated high-resolution solution at the coarse (low-resolution) grid points.

For training our neural closure models for the low-resolution discretization with  $N_x = 25$ , we use the same training regiment as in Experiments-1 (Sec. 4.1), comparing the same three closures: no-delays (nODEs), discrete-delays (discrete-nDDE), and distributed-delays (distributed-nDDE) with architectures details presented in Table 2. For the nODE, we again employ a substantially wider and deeper architecture with more trainable parameters, and for the discrete-nDDE, only two discrete delay values are again used. The training period still ranges from  $t = 0$  to 1.25 and the prediction period from  $t = 1.25$  to 2.5. For these experiments-2, we use: a batch size of 8 created by randomly selecting short time-sequences spanning 6 time-steps and extracting data at every other time-step; 4 iterations per epoch; exponentially decaying learning rate (LR) schedule with initial LR of 0.075, decay rate of 0.97, and 4 decay steps; *RMSprop* optimizer; time-averaged  $L_2$  error as the loss function; and end training at 150 epochs. For time-integration, we use the *Vode* scheme [11]. The true data are generated by interpolating the high-resolution solution onto the low-resolution grid, as shown in Fig. 7c.

The performance of the three neural closure models after 150 epochs (the stochastic gradient descent nearly converges, as evident from Fig. 9) is evaluated by taking the absolute difference with the high-resolution solution interpolated onto the low-resolution grid (Fig. 7c) spanning both the training and prediction periods. We further benchmark our performance against the popular Smagorinsky model used for turbulence closure [57], which introduces a turbulent eddy viscosity ( $\nu_e$ ) to the Burger’s equation (Eq. 23),

$$\frac{\partial u}{\partial t} + u \frac{\partial u}{\partial x} = \nu \frac{\partial^2 u}{\partial x^2} + \frac{\partial}{\partial x} \left( \nu_e \frac{\partial u}{\partial x} \right), \quad (28)$$

where  $\nu_e = (C_s \Delta x)^2 \left| \frac{\partial u}{\partial x} \right|$  and  $C_s$  is the Smagorinsky constant. Results are shown in Fig. 8, and details of the architectures used to produce these results are given in Table 2. As shown by the error fields of the baseline (Fig. 7d) and closure models (Fig. 8), and by the corresponding pairs of averaged error numbers (see Figs.), all closures improve the baseline. However, the nODE and Smagorinsky closures only lead to a 40-50% decrease in error, while the nDDE closures achieve a 65-70% decrease. Despite the wider and deeper architecture for the nODE, both the discrete-nDDE and distributed-nDDE (with smaller architectures) again achieve smaller errors, for the whole period of  $t = 0$  to 2.5. This means that they have lower numerical diffusion, thus capturing the targeted subgrid-scale process. We also find that the discrete-nDDE performs slightly better than the distributed-nDDE in the training period, while the opposite occurs for the prediction period. These results are corroborated from the progression with training epochs of the time-averaged  $L_2$  loss, for both training and prediction periods.

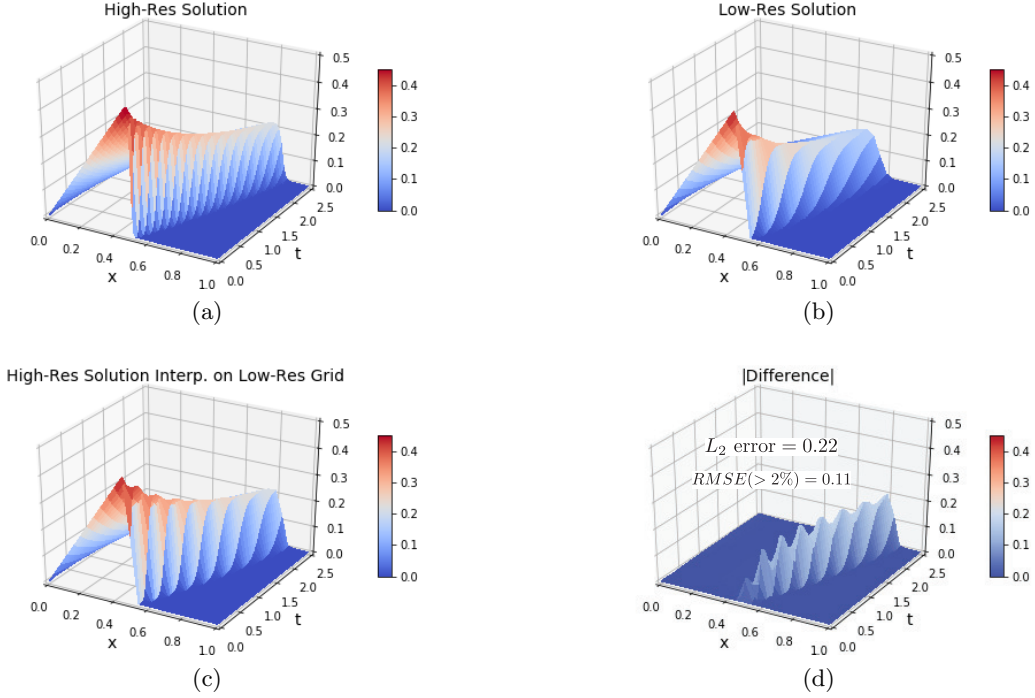
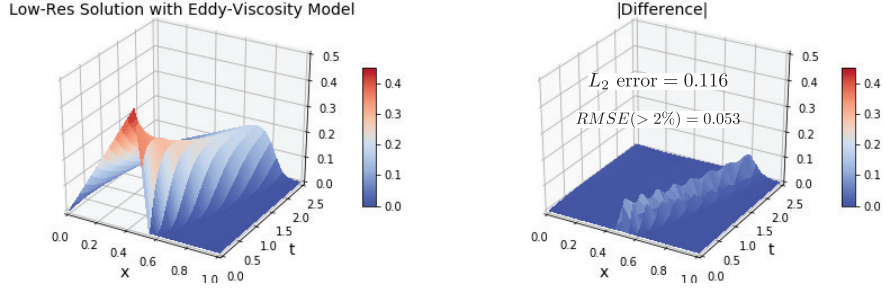


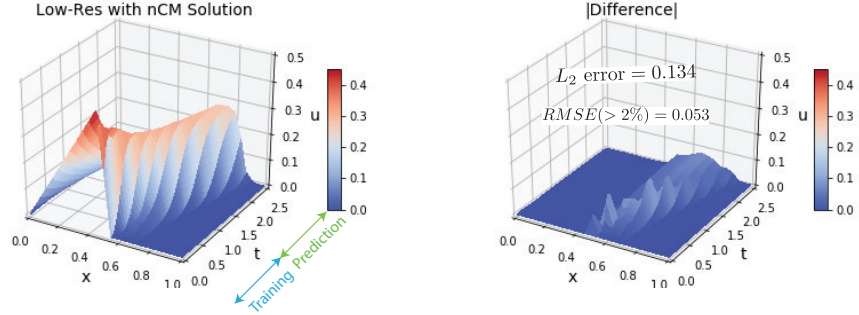
Figure 7: Comparison of solutions of Burger’s equation (Eq. 23) for different grid resolutions. (a): Solution for a high-resolution grid with number of grid points,  $N_x = 100$ ; (b): Solution for a low-resolution grid with  $N_x = 25$ ; (c): High-resolution solution interpolated onto the low-resolution grid. (d): Absolute difference between fields in panels (b) and (c). We also provide a pair of time-averaged errors, specifically:  $L_2$  error; and RMSE considering only the grid points where the error is at least 2% of the maximum velocity value, denoted by  $RMSE(>2\%)$ .

Category	Architecture	Act.	Delays	Trainable Parameters
nODE (No-Delays)	$f_{NN}$			
	Input layer with 25 neurons	none	None	2725
	5 FC hidden layer with 20 neurons	tanh		
FC output layer with 20 neurons	linear			
Discrete-nDDE	$f_{RNN}$			
	Input layer with 25 neurons	none	$\tau_1 =$	745
	Simple RNN layer with 10 neurons	tanh	0.025,	
	FC hidden layer with 10 neurons	tanh	$\tau_2 = 0.05$	
FC output layer with 25 neurons	linear			
Distributed-nDDE	$f_{NN}$			
	Input layer with 28 neurons	none	$\tau_1 = 0,$ $\tau_2 = 0.075$	853
	2 FC hidden layer with 10 neurons	tanh		
	FC output layer with 25 neurons	linear		
	$g_{NN}$			
Input layer with 25 neurons	none			
2 FC hidden layer with 5 neurons	tanh			
FC output layer with 3 neurons	linear			

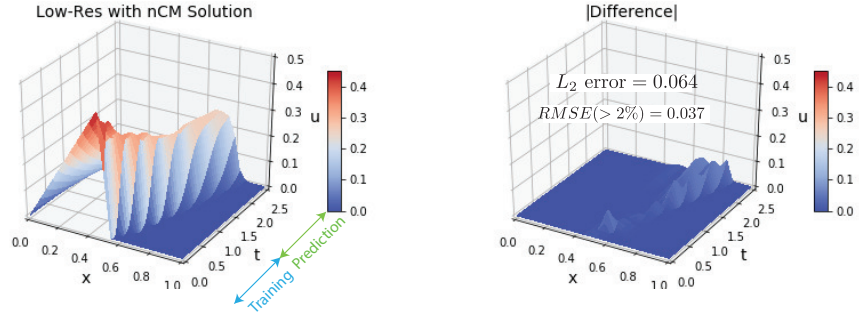
Table 2: Architectures for different neural closure models used in Experiments-2. FC stands for fully-connected and the last column notes the number of trainable parameters available.



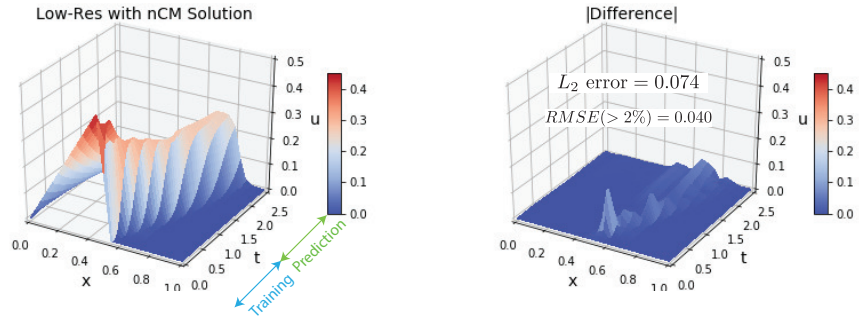
(a) Smagorinsky model



(b) nODE



(c) Discrete-nDDE



(d) Distributed-nDDE

Figure 8: Solutions of the Burger's PDE on the low-resolution grid with different closure models (*left-column*), and their absolute differences (*right-column*) with the high-resolution solution interpolated onto the low-resolution grid (Fig. 7c). For the trained neural closure models, the training period is from  $t = 0$  to 1.25 while the prediction period is from  $t = 1.25$  to 2.5. For each closure, we also provide the pair of time-averaged errors (see Fig. 7 for description). (a): Smagorinsky model with  $C_s = 1.0$ ; (b): neural ODEs with no-delays (nODE); (c): neural DDEs with discrete-delays (Discrete-nDDE); (d): neural DDEs with distributed-delays (Distributed-nDDE). These results correspond to the architectures detailed in Table 2.

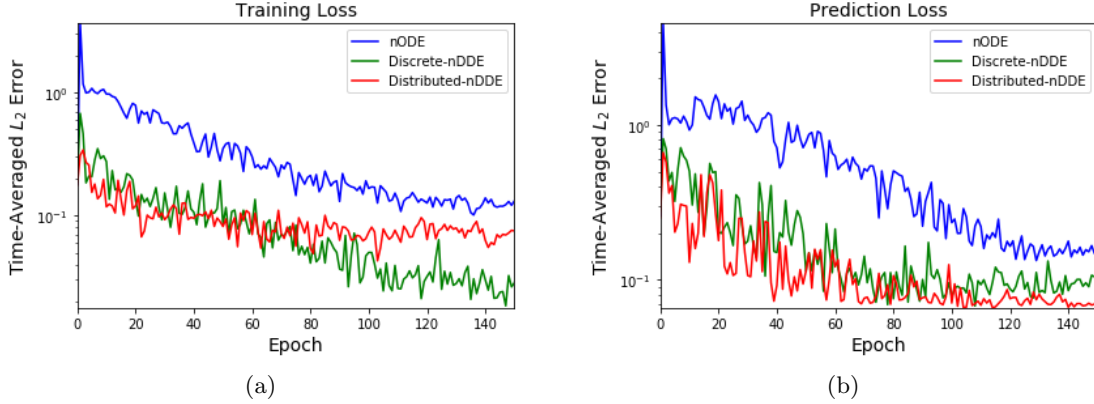


Figure 9: Variation with epochs of (a): training; and (b): prediction time-averaged  $L_2$  error loss for the three neural closure models, while training for Experiments-2. These results accompany Figure 8 and the architectures detailed in Table 2.

As for experiments-1, we conducted a series of experiments-2, to study the effect of changing the amount of past information incorporated in the neural closure models. In Fig. 6b, we show the variation the average prediction loss (time-averaged  $L_2$  error) between the last epochs 120 to 150, for different delay-period lengths ( $\tau_1 = 0$ , and  $\tau_2$  varying in case of distributed-nDDE). We again find an optimal memory length for a specified architecture. We further conducted other experiments-2 to assess the sensitivity to the various other hyperparameters, and found similar trends (not shown here) as in the experiments-1. Finally, we noticed that using the *dopri5* [34] time-integration scheme severely impaired the learning ability in the experiments-2.

Overall, these results demonstrate the superiority of using our new memory-based closure models in capturing subgrid-scale processes.

### 4.3 Experiments 3: Marine Biogeochemical Models

For our third experiments, we use neural closure models to incorporate the effects of missing processes and state variables in low-complexity biogeochemical models, thus targeting the third class of dynamical systems which require closure modeling (Sec. 2.3). Marine biogeochemical models are a set of ODEs that describe the food-web interactions in the ecosystem. This is a domain where models can vary greatly in terms of complexity [25]. The marine biogeochemical models used in these experiments are adapted from Newberger et. al., 2003 ([63]). These models were used to simulate the ecosystem in the Oregon coastal upwelling zone in a two-dimensional approximation. They provide hierarchical embedded models compatible with each other. We employ the three-component NPZ model (nutrients ( $N$ ), phytoplankton ( $P$ ), and zooplankton ( $Z$ )), and the five-component NNPZD model (ammonia ( $NH_4$ ), nitrate ( $NO_3$ ),  $P$ ,  $Z$ , and detritus ( $D$ )). The low complexity NPZ model is given by,

$$\begin{aligned}
 \frac{dN}{dt} &= -G \frac{PN}{N + K_u} + \Xi P + \Gamma Z + R_m \gamma Z (1 - \exp^{-\Lambda P}) \\
 \frac{dP}{dt} &= G \frac{PN}{N + K_u} - \Xi P - R_m Z (1 - \exp^{-\Lambda P}) \\
 \frac{dZ}{dt} &= R_m (1 - \gamma) Z (1 - \exp^{-\Lambda P}) - \Gamma Z \\
 N(0) &= T_{bio}, \quad P(0) = 0, \quad \text{and} \quad Z(0) = 0
 \end{aligned} \tag{29}$$

with  $G$  representing the optical model,

$$G = V_m \frac{\alpha I}{(V_m^2 + \alpha^2 I^2)^{1/2}}, \quad \text{and} \quad I(z) = I_0 \exp(k_w z), \tag{30}$$

where  $z$  is depth and  $I(z)$  models the availability of sunlight for photo-chemical reactions. The parameters in Eqs. 29 and 30 are:  $k_w$ , light attenuation by sea water;  $\alpha$ , initial slope of the  $P - I$  curve;  $I_0$ , surface photosynthetically available radiation;  $V_m$ , phytoplankton maximum uptake rate;  $K_u$ , half-saturation for phytoplankton uptake of nutrients;  $\Xi$ , phytoplankton specific mortality rate;  $R_m$ , zooplankton maximum grazing rate;  $\Lambda$ , Ivlev constant;  $\gamma$ , fraction of zooplankton grazing egested;  $\Gamma$ , zooplankton specific excretion/mortality rate; and  $T_{bio}$ , total biomass concentration. In the NPZ model (Eq. 29), the nutrient uptake by phytoplankton is governed by a Michaelis-Menten formulation, which amounts to a linear uptake relationship at low nutrient concentrations that saturates to a constant at high concentrations. The grazing of phytoplankton by zooplankton follows a similar behavior: their growth rate becomes independent of  $P$  in case of abundance, but proportional to available  $P$  when resources are scarce, hence zooplankton grazing is modeled by an Ivlev function. The death rates of both  $P$  and  $Z$  are linear, and a portion of zooplankton grazing in the form of excretion goes directly to nutrients.

In the higher complexity NNPZD model, the nutrients are divided into ammonia and nitrates, which are the two most important forms of nitrogen in the ocean. With the intermediate of decomposed organic matter, detritus, the NNPZD model captures new processes such as: phytoplankton cells preferentially taking up ammonia over nitrate because the presence of ammonia inhibits the activity of the enzyme nitrate reductase essential for the uptake kinetics; the pool of ammonium coming from remineralization of detritus; and part of this ammonium pool getting oxidized to become a source of nitrate called the process of nitrification, etc. Overall, the NNPZD model is given by,

$$\begin{aligned}
\frac{dNO_3}{dt} &= \Omega NH_4 - G \left[ \frac{NO_3}{NO_3 + K_u} \exp^{-\Psi NH_4} \right] P \\
\frac{dNH_4}{dt} &= -\Omega NH_4 + \Phi D + \Gamma Z - G \left[ \frac{NH_4}{NH_4 + K_u} \right] P \\
\frac{dP}{dt} &= G \left[ \frac{NO_3}{NO_3 + K_u} \exp^{-\Psi NH_4} + \frac{NH_4}{NH_4 + K_u} \right] P - \Xi P \\
&\quad - R_m Z (1 - \exp^{-\Lambda P}) \\
\frac{dZ}{dt} &= R_m (1 - \gamma) Z (1 - \exp^{-\Lambda P}) - \Gamma Z \\
\frac{dD}{dt} &= R_m \gamma Z (1 - \exp^{-\Lambda P}) + \Xi P - \Phi D \\
NO_3(0) &= T_{bio}/2, \quad NH_4(0) = T_{bio}/2, \quad P(0) = 0, \\
Z(0) &= 0, \quad \text{and } D(0) = 0
\end{aligned} \tag{31}$$

where the new parameters are:  $\Psi$ ,  $NH_4$  inhibition parameter;  $\Phi$ , detritus decomposition rate; and  $\Omega$ ,  $NH_4$  oxidation rate.

Solutions of the above two models are presented in Fig. 10. Different values of the parameters and initial conditions set these models in different dynamical regimes. As we observe from the responses in time, the present solutions in experiments-3 are in a stable nonlinear limit-cycle regime. The  $N$  class in the NPZ model is a broader class encompassing  $NO_3$ ,  $NH_4$ , and  $D$  from the NNPZD model. Since the NNPZD model resolves many more processes, the concentrations of  $NO_3 + NH_4 + D$ ,  $P$ , and  $Z$  differ significantly from the  $N$ ,  $P$ , and  $Z$  of the NPZ model. The goal of the neural closure models in these experiments is thus to augment the low-complexity NPZ model such that it matches the aggregated states of the high-complexity NNPZD model.

For training our neural closure models for the NPZ model, we use the same training regiment as in Experiments-1 & 2 (Secs. 4.1 & 4.2), comparing the same three closures: no-delays (nODEs), discrete-delays (discrete-nDDE), and distributed-delays (distributed-nDDE) with architectures details presented in Table 3. For the nODE, we again employ a bigger architecture, and for the for discrete-nDDE, only two discrete delay values are again used. The training period ranges from  $t = 0$  to 20 days and the prediction period from  $t = 20$  to 40 days. For these experiments-3, we use: a batch size of 8 created by randomly selecting short time-sequences spanning 6 time-steps and extracting data at every other time-step; 10 iterations per epoch; exponentially decaying learning rate (LR) schedule with initial LR of 0.05, decay rate of 0.97, and 10 decay steps; *RMSprop* optimizer; and end training at 200 epochs. For biological models, there exists

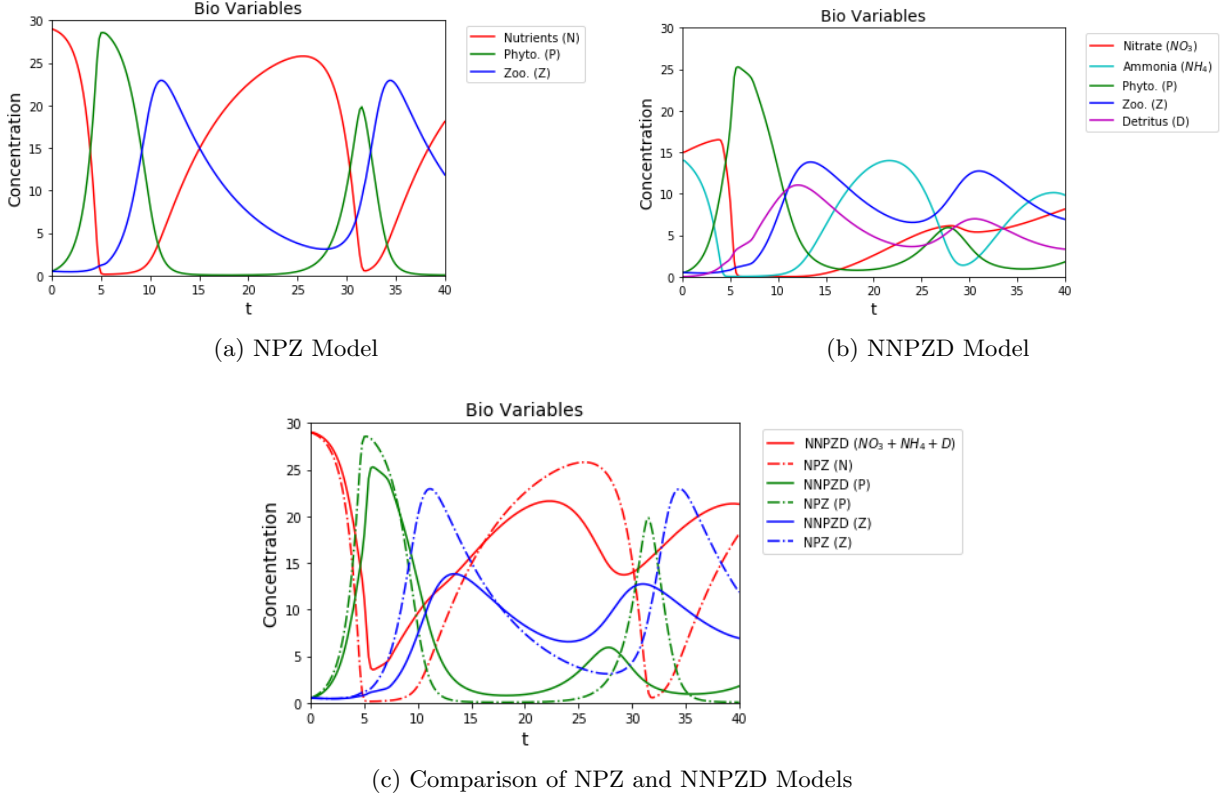


Figure 10: Solutions of the marine biogeochemical models used in Experiments-3 (concentrations vs. time in *days*). Parameter values used are (adopted from [63]):  $k_w = 0.067 \text{ m}^{-1}$ ,  $\alpha = 0.025 \text{ (W m}^{-2} \text{ d)}^{-1}$ ,  $V_m = 1.5 \text{ d}^{-1}$ ,  $I_0 = 158.075 \text{ W m}^{-2}$ ,  $K_u = 1 \text{ mmol N m}^{-3}$ ,  $\Psi = 1.46 \text{ (mmol N m}^{-3})^{-1}$ ,  $\Xi = 0.1 \text{ d}^{-1}$ ,  $R_m = 1.5 \text{ d}^{-1}$ ,  $\Lambda = 0.06 \text{ (mmol N m}^{-3})^{-1}$ ,  $\gamma = 0.3$ ,  $\Gamma = 0.145 \text{ d}^{-1}$ ,  $\Phi = 0.175 \text{ d}^{-1}$ ,  $\Omega = 0.041 \text{ d}^{-1}$ ,  $z = -15 \text{ m}$ , and  $T_{bio} = 30 \text{ mmol N m}^{-3}$ . (a): Nutrient-Phytoplankton-Zooplankton (NPZ) model (Eq. 29); (b): Nitrate-Ammonia-Phytoplankton-Zooplankton-Detritus (NNPZD) model (Eq. 31); (c): Comparison between  $NO_3 + NH_4 + D$ ,  $P$ , and  $Z$  from the NNPZD model (*solid*) with  $N$ ,  $P$  and  $Z$  from the NPZ model (*dashed-dot*).

Category	Architecture	Act.	Delays	Trainable Parameters	
nODE (No-Delays)	$f_{NN}$		None	276	
	Input layer with 3 neurons	none			
	5 FC hidden layer with 7 neurons	tanh			
	FC output layer with 3 neurons	linear			
Discrete-nDDE	$f_{RNN}$		$\tau_1 = 1.5,$ $\tau_2 = 3.0$	157	
	Input layer with 3 neurons	none			
	Simple RNN layer with 7 neurons	tanh			
	FC hidden layer with 7 neurons	tanh			
	FC output layer with 3 neurons	linear			
Distributed-nDDE	$f_{NN}$		$\tau_1 = 0,$ $\tau_2 = 2.0$	210	
	Input layer with 7 neurons	none			
	2 FC hidden layer with 7 neurons	tanh			
	FC output layer with 3 neurons	linear			
	$g_{NN}$				
	Input layer with 3 neurons	none			
	2 FC hidden layer with 5 neurons	tanh			
	FC output layer with 4 neurons	linear			

Table 3: Architectures for different neural closure models used in Experiments-3. FC stands for fully-connected and the last column notes the number of trainable parameters available.

invariant knowledge about the system, such as biological state variables cannot be negative, and the sum of all the states remains constant with time (this can be verified by adding the ODEs of NPZ or NNPZD models). Thus, we incorporate penalization for these two properties in the loss function along with the standard time-averaged  $L_2$  error w.r.t. to the true data. The true data are generated by aggregating the variables of the NNPZD model ( $N \equiv NO_3 + NH_4 + D$ ,  $P$ , and  $Z$ ). Finally, we use *dopri5* [34] scheme with a time-step size of  $\Delta t = 0.05$  for all our time-integration requirements.

The performance of the three neural closure models augmenting the NPZ is evaluated after 200 epochs of training (the stochastic gradient descent nearly converges, as evident from Figure 12) by comparison with the aggregated biology variables from the high-complexity NNPZD model (Eq. 31) spanning both the training and prediction periods. Results are presented in Figure 11. The details of the architectures used to produce these results are given in Table 3. When compared with the aggregated NNPZD variables (true variables), we find again that despite the bigger architecture for the nODE case, it leads to significant errors during both the training and prediction periods, and large deviations around the peaks between  $t = 25$  to  $30$  days. The discrete-nDDE and distributed-nDDE, both with smaller architectures, are able however to match the true variables for nearly the whole period of  $t = 0$  to  $40$  days, with smaller deviations around the peaks between  $t = 25$  to  $30$  days. Both discrete-nDDE and distributed-nDDE perform equally well in both training and prediction periods. These results are corroborated from the progression with training epochs of the time-averaged  $L_2$  loss (here, the error between the variables from the closure-model-augmented NPZ system, and the true variables), for both training and prediction periods. We notice very large spikes in the first quarter of the training regime, which are due to weights of the neural-networks taking values that lead to negative biology variables. As training progresses, we however don't observe this behavior anymore because the penalization included in the loss function avoids this. In conclusion, using a memory based closure for a low-complexity model can efficiently help emulate the high-complexity model dynamics.

As in prior experiments, we conducted a series of experiments-3 to study the effect of changing the amount of past information incorporated in the neural closure models as well as the sensitivity to the various hyperparameters. We found similar trends (not shown here) as in experiments-1&2. For good performance, we further found that using a small enough time-step was critical as well as limiting the number of internal steps in the *dopri5* [34] time-integration scheme.

In general, the biogeochemical ODEs are coupled with regional or global ocean modeling systems, leading to advection-diffusion-reaction PDEs [4]. If highly complex biogeochemical-ecosystem models are employed,

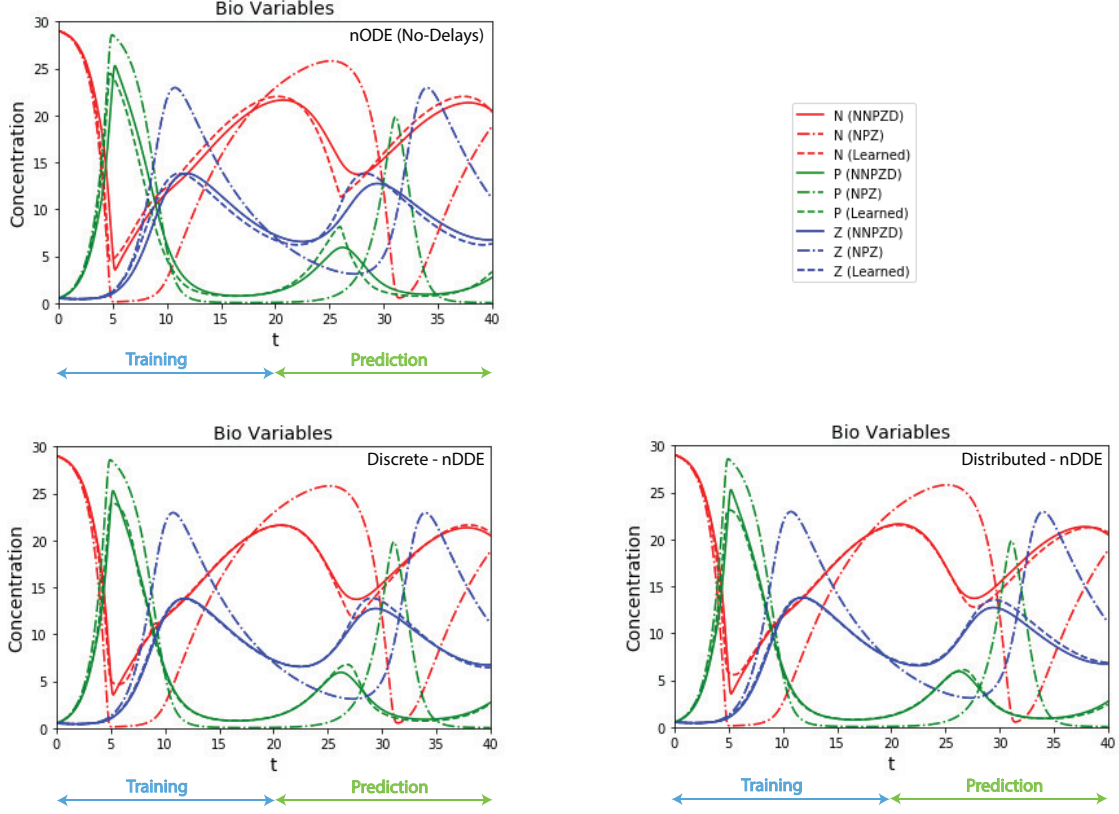


Figure 11: Comparison of the biogeochemical variables from the learned NPZ model augmented with the three neural closure models (*dashed*), aggregated variables from the NNPZD model (*solid*), and variables from the NPZ model (*dashed-dot*) at the end of training. For each neural closure, the training period is from  $t = 0$  to 20 days while prediction period is from  $t = 20$  to 40 days. *Top-left*: neural ODEs with no-delays (nODE); *bottom-left*: neural DDEs with discrete-delays (Discrete-nDDE); *bottom-right*: neural DDEs with distributed-delays (Distributed-nDDE). These results correspond to the architectures detailed in Table 3.

a very large number of PDE state variables need to be solved for, rendering the computations very expensive. A large number of unknown parameter values as well as uncertain initial conditions then also need to be estimated, requiring specific methods [e.g. 50]. The available biogeochemical observations are not always sufficient for calibrating these many unknown parameters and for estimating initial conditions of high-complexity models. If the corresponding errors are large, this can lead to integrating models in the wrong dynamical regimes [e.g. 88]. Finally, in some applications, one is only interested in the aggregated state variables as the output, but cannot use low-complexity models because their dynamics are too inaccurate for the goals of the applications. Using neural closure models as shown here, one can increase the accuracy of the low-complexity models to match the response of high-complexity models (possibly up to models such as ERSEM [3]) without adding the computational burden of modeling all the intermediate biological states and processes.

#### 4.4 Computational Complexity

It is crucial to analyze complexity and in particular the cost of adding a neural closure model to a low-fidelity model. In this section, we analyze the computational complexity in terms of *flop* (floating point operations) count for evaluating the right-hand-side (RHS) of the low-fidelity models, and for the forward-pass of the neural closure models [62]. We will also comment on the training costs. The Burger’s PDE considered for Experiments 1&2 (Sec. 4.1&4.2) has a nonlinear advection term. Hence, for the POD-GP ROM and the FOM, the upper *flops* is of the order of the square of number of resolved modes and of the spatial grid

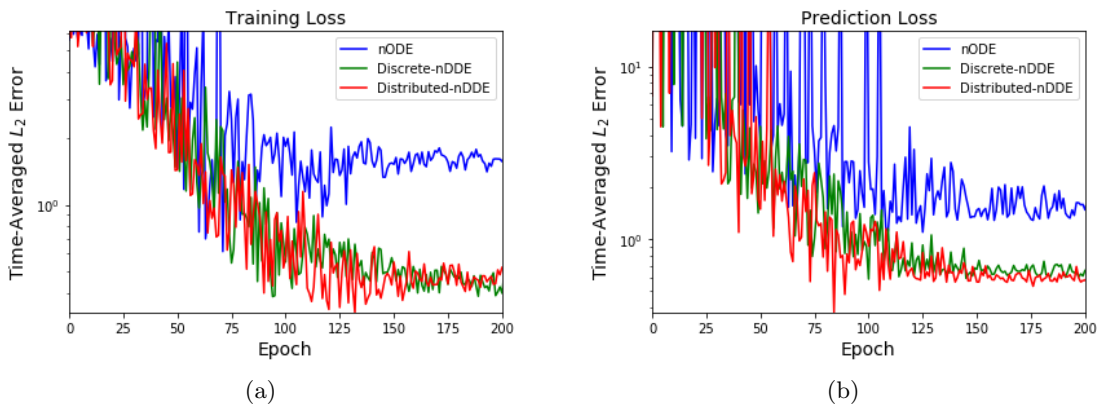


Figure 12: Variation with epochs of (a): training; and (b): prediction time-averaged  $L_2$  loss for the three neural closure models, while training for Experiment-3. These results accompany Figure 11 and the architectures detailed in Table 3.

resolution, respectively. In general, for reaction terms and biogeochemical systems, the number of nonlinear parameterizations present are of the order of the number of state variables in the model. Hence, even for Experiments 3 (Sec. 4.3), the upper *flops* is of the order of the square of the number of biological components. Let the number of state variables in the low-fidelity models be  $N \in \mathbb{N}$ , thus the leading order computational complexity would be  $\mathcal{O}(cN^2)$ , where  $c \in \mathbb{R}^+$  is some constant dependent on the numerical schemes used for spatial discretization, the exact functional form of the RHS, etc.

Now, when neural closure models are added to the low-fidelity models, the time integration requires a forward pass through the neural-network. This cost varies with the neural architecture and model type, here either a discrete-nDDE or distributed-nDDE. As observed in our experiments, using delays in the closure model enables us to use shallower networks, with a depth independent of the number of state variables ( $N$ ). We also found that the width of the networks was similar to, or smaller than,  $N$ . In case of distributed-nDDEs, we observed that the width of the auxiliary network ( $g_{NN}$ ) could be on an average nearly half the size of the main network ( $f_{NN}$ ). Let the size of the hidden state for the RNN in discrete-nDDEs be  $N_h \in \mathbb{N}$ , and the number of neurons in the hidden layers of the main and auxiliary networks in the case of distributed-nDDEs be  $N_h$  and  $N_h/2$ , respectively, with  $N_h \lesssim N$ . It could be easily shown that the leading order complexity for a single iteration of RNN would be  $\mathcal{O}(N_h^2 + N_h N)$ , which is due to the hidden and input state vectors being multiplied by the weight matrices, while the application of activation function would be  $\mathcal{O}(N_h)$  only. As the number of discrete-delays in discrete-nDDEs are independent of  $N$  and  $\mathcal{O}(1)$ , it does not affect the complexity of the RNN. The complexity of the first hidden layer and/or the output layer of the deep neural-networks used in discrete-nDDEs and distributed-nDDEs (main network,  $f_{NN}$ ) will be  $\mathcal{O}(N_h N)$  and  $\mathcal{O}(N_h(N + N_h/2))$ , respectively, while for the remaining hidden layers, it will be  $\mathcal{O}(N_h^2)$ . Focusing on the integral of the auxiliary network ( $g_{NN}$ ) over the delay period in distributed-nDDEs, if implemented efficiently, at every time-step, we only need to compute the integral twice over periods of size  $\Delta t$ , each adjacent to the ends of the present delay-period. We can add and subtract these integrals over  $\Delta t$  periods to compute the overall integral in a rolling window sense. Hence, the contribution to the computational cost by the auxiliary network would be  $\mathcal{O}(N_h N/2)$  (for first hidden layer) and  $\mathcal{O}(N_h^2/4)$  (subsequent hidden layers). Considering  $D \in \mathbb{N}$  as the depth for all the different types of networks considered, the complexity for the forward pass through the discrete-nDDE closure is  $\mathcal{O}(DN_h^2 + DN_h N)$ , while for distributed-nDDE, it is  $\mathcal{O}((3/2)N_h N + (7/4)DN_h^2)$ . Thus, the additional computational cost due to the presence of neural closure models is of similar or lower complexity than the existing low-fidelity model.

Estimating the computational cost/complexity of training in *flops* is not common because apart from time-integrating the forward model and adjoint equations, there are many other operations such as here: automatic differentiation through the neural networks; creation and use of interpolation functions; the integral to compute the final derivatives; the gradient descent step, etc. The overall cost also depends on the number of epochs needed for convergence. The present training cost is of course non-negligible, as with any

supervised learning algorithm. However, in applications where one needs to repeatedly solve a low-fidelity model, investing in a one-time cost of training a neural closure model can later lead to accuracy close to that of the high-fidelity model with only a small increase in the computational cost of the low-fidelity model.

## 5 Conclusion

We developed a novel, versatile, and rigorous methodology to learn closure parameterizations for low-fidelity models using data from high-fidelity simulations. The Mori-Zwanzig formulation [85, 18, 33], and the presence of inherent delays in many natural dynamical systems (especially biological systems [32, 87]), justify the need for non-Markovian closure parameterizations. To that effect, our framework, *neural closure models*, extends neural ordinary differential equations (nODEs; [16]) to neural delay differential equations (nDDEs) to model and learn such non-Markovian closures. This approach does not require access to the high-fidelity model or frequent enough high-fidelity data to be able to compute the time derivative of the state with a high accuracy. Further, it enables the accounting of errors in the time-evolution of the states in the presence of neural networks during training. We also provide adjoint equation derivations and network architectures needed to efficiently implement the nDDEs, for both discrete and distributed delays. In the case of discrete delays, we propose the use of recurrent architectures, while for distributed delays, coupled deep neural network architectures.

Through simulation experiments, we demonstrate that our methodology drastically improves the predictive capability of low-fidelity models for the three main classes of model truncations. Specifically, our neural closure models efficiently account for truncated modes in reduced-order-models (ROMs), capture the effects of subgrid-scale processes in coarse models, and augment the simplification of complex mathematical models. Our first two classes of simulation experiments utilize the advecting shock problem governed by the Burger’s PDE, with its low-fidelity models derived either using proper-orthogonal-decomposition Galerkin projection or reducing the spatial grid resolution. Our third class of experiments considers marine biogeochemical models of varying complexities, with low-fidelity models obtained by aggregation of components and other simplifications of ecosystem processes and parameterizations. In each of these three experiments, we consistently show that using non-Markovian over Markovian closures improves the accuracy of the learned system while also requiring smaller network architectures. These results are obtained using stringent evaluations: in all the experiments, we compare the performance of the learned system for the training period (period for which high-fidelity data snapshots are used for training) as often done, but we also compare it for longer-term predictions. Specifically, even for a prediction period that is of the same length as the training period and has no overlap with it, the nDDE closures remain very successful.

In our experiments, we find that just using a few numbers of discrete delays might perform equally well or better than using a distributed delay which involves an integral of the state variable over a delay period. We provide a plausible explanation of this counter-intuitive observation using the data processing inequality from information theory. We also show that there exists an optimal amount of past information to incorporate for a specified architecture, thus indicating that neither too little nor too much past information is helpful. Finally, a computational complexity analysis using *flop* (floating point operation) count proves that the additional computational cost due to the presence of our neural closure models is of similar or lower complexity than the existing low-fidelity model.

The present work provides a general framework to learn non-Markovian closure parameterization using neural networks. It also enables the use of the often elusive Mori-Zwanzig formulation [85, 18, 33] in its full glory without unjustified approximations and simplifications. The applications of our nDDE closures are not just limited to the shown experiments, but could be widely extended to other fields such as, control theory, robotics, pharmacokinetic-pharmacodynamics, chemistry, economics, biological regulatory systems, etc.

**Data Accessibility.** The codes and data used in this work are available on request from the authors.

**Author’s Contributions.** A.G. conceived the idea of using neural delay differential equations for closure parameterizations; derived the adjoint equations; implemented the neural network architectures and the simulation experiments; interpreted the computational results; and wrote a first draft of the manuscript. P.F.J.L. supervised the work; conceived the ideas to extend the methodology to capture the effects of

subgrid-scale processes in coarse models, and to augment the simplification of complex mathematical models; interpreted the computational results; and edited and wrote parts of the manuscript.

**Competing Interests.** We declare we have no competing interests.

**Funding.** We are grateful to the Office of Naval Research for partial support under grant N00014-20-1-2023 (MURI ML-SCOPE) to the Massachusetts Institute of Technology. We also thank MathWorks and the Mechanical Engineering Department at MIT for awarding a competitive 2020-2021 MathWorks Mechanical Engineering Fellowship for A.G. Some of the computations were made possible due the Google Cloud Platform research credits, which we gratefully acknowledge.

**Acknowledgement.** We thank the members of our MSEAS group for their collaboration and insights, especially Mr. Aaron Charous. We also thank our ML-SCOPE team for many useful discussions, especially Dr. Mickaël Chekroun for his comments on the final draft of the manuscript.

## References

- [1] M. Abadi, , et al. TensorFlow: Large-scale machine learning on heterogeneous systems, 2015. URL <https://www.tensorflow.org/>. Software available from tensorflow.org.
- [2] G. Alfonsi. Reynolds-averaged navier–stokes equations for turbulence modeling. *Applied Mechanics Reviews*, 62(4), 2009.
- [3] J. Baretta, W. Ebenhöf, and P. Ruardij. The European regional seas ecosystem model, a complex marine ecosystem model. *Netherlands Journal of Sea Research*, 33(3-4):233–246, 1995.
- [4] Ş. T. Beşiktepe, P. F. J. Lermusiaux, and A. R. Robinson. Coupled physical and biogeochemical data-driven simulations of Massachusetts Bay in late summer: Real-time and post-cruise data assimilation. *J. of Marine Systems*, 40–41:171–212, 2003. doi: 10.1016/S0924-7963(03)00018-6.
- [5] F. Behzad, B. T. Helenbrook, and G. Ahmadi. On the sensitivity and accuracy of proper-orthogonal-decomposition-based reduced order models for Burgers equation. *Computers & Fluids*, 106:19–32, 2015.
- [6] K. Bhattacharya, M. Ghil, and I. Vulis. Internal variability of an energy-balance model with delayed albedo effects. *Journal of the Atmospheric Sciences*, 39(8):1747–1773, 1982.
- [7] Board - Ocean Studies and National Academies of Sciences, Engineering, and Medicine and others. *Next generation earth system prediction: strategies for subseasonal to seasonal forecasts*. National Academies Press, 2016.
- [8] G. A. Bocharov and F. A. Rihan. Numerical modelling in biosciences using delay differential equations. *Journal of Computational and Applied Mathematics*, 125(1-2):183–199, 2000.
- [9] N. Boers, M. D. Chekroun, H. Liu, D. Kondrashov, D.-D. Rousseau, A. Svensson, M. Bigler, and M. Ghil. Inverse stochastic–dynamic models for high-resolution greenland ice core records. *Earth System Dynamics*, 8(4):1171–1190, 2017. doi: 10.5194/esd-8-1171-2017.
- [10] A. Borja et al. Tales from a thousand and one ways to integrate marine ecosystem components when assessing the environmental status. *Frontiers in Marine Science*, 1:72, 2014.
- [11] P. N. Brown, G. D. Byrne, and A. C. Hindmarsh. VODE: A variable-coefficient ODE solver. *SIAM journal on scientific and statistical computing*, 10(5):1038–1051, 1989.
- [12] S. L. Brunton, J. L. Proctor, and J. N. Kutz. Discovering governing equations from data by sparse identification of nonlinear dynamical systems. *PNAS*, 113(15):3932–3937, 2016.
- [13] J. Calver and W. Enright. Numerical methods for computing sensitivities for ODEs and DDEs. *Numerical Algorithms*, 74(4):1101–1117, 2017.

- [14] E. P. Chassignet and J. Verron. *Ocean modeling and parameterization*, volume 516. Springer Science & Business Media, 2012.
- [15] M. D. Chekroun, H. Liu, and J. C. McWilliams. Variational approach to closure of nonlinear dynamical systems: Autonomous case. *Journal of Statistical Physics*, pages 1–88, 2019.
- [16] T. Q. Chen, Y. Rubanova, J. Bettencourt, and D. K. Duvenaud. Neural ordinary differential equations. In *Advances in neural information processing systems*, pages 6571–6583, 2018.
- [17] Y. Choi and K. Carlberg. Space–time least-squares Petrov–Galerkin projection for nonlinear model reduction. *SIAM Journal on Scientific Computing*, 41(1):A26–A58, 2019.
- [18] A. J. Chorin, O. H. Hald, and R. Kupferman. Optimal prediction and the Mori–Zwanzig representation of irreversible processes. *PNAS*, 97(7):2968–2973, 2000.
- [19] T. M. Cover. *Elements of information theory*. John Wiley & Sons, 1999.
- [20] D. P. Dauhajre, J. C. McWilliams, and L. Renault. Nearshore lagrangian connectivity: submesoscale influence and resolution sensitivity. *Journal of Geophysical Research: Oceans*, 124(7):5180–5204, 2019.
- [21] T. Daulbaev, A. Katrutsa, L. Markeeva, J. Gusak, A. Cichocki, and I. Oseledets. Interpolation technique to speed up gradients propagation in neural ODEs. *Advances in Neural Information Processing Systems*, 33, 2020.
- [22] L. Dell’Anna. Solvable delay model for epidemic spreading: the case of covid-19 in italy. *Scientific Reports*, 10(1), Sept. 2020. doi: 10.1038/s41598-020-72529-y.
- [23] O. Diekmann, S. A. Van Gils, S. M. Lunel, and H.-O. Walthers. *Delay equations: functional-, complex-, and nonlinear analysis*, volume 110. Springer Science & Business Media, 2012.
- [24] B. Faugeras and O. Maury. Modeling fish population movements: from an individual-based representation to an advection–diffusion equation. *J. of Theoretical Biology*, 247(4):837–848, 2007.
- [25] W. Fennel and T. Neumann. *Introduction to the modelling of marine ecosystems*. Elsevier, 2014.
- [26] F. Feppon and P. F. J. Lermusiaux. A geometric approach to dynamical model-order reduction. *SIAM Journal on Matrix Analysis and Applications*, 39(1):510–538, 2018. doi: 10.1137/16M1095202.
- [27] F. Feppon and P. F. J. Lermusiaux. Dynamically orthogonal numerical schemes for efficient stochastic advection and Lagrangian transport. *SIAM Review*, 60(3):595–625, 2018. doi: 10.1137/16M1109394.
- [28] B. Fox-Kemper and D. Menemenlis. Can large eddy simulation techniques improve mesoscale rich ocean models. *Ocean modeling in an eddying regime*, 177:319–337, 2008.
- [29] B. Fox-Kemper, A. Adcroft, C. W. Böning, E. P. Chassignet, E. Curchitser, G. Danabasoglu, C. Eden, M. H. England, R. Gerdes, R. J. Greatbatch, et al. Challenges and prospects in ocean circulation models. *Frontiers in Marine Science*, 6:65, 2019.
- [30] M. Ghil, M. D. Chekroun, and G. Stepan. A collection on ‘climate dynamics: multiple scales and memory effects’, 2015.
- [31] A. Gholami, K. Keutzer, and G. Biros. Anode: Unconditionally accurate memory-efficient gradients for neural odes. *arXiv preprint arXiv:1902.10298*, 2019.
- [32] D. S. Glass, X. Jin, and I. H. Riedel-Kruse. Nonlinear delay differential equations and their application to modeling biological network motifs. *BioRxiv*, 2020.
- [33] A. Gouasmi, E. J. Parish, and K. Duraisamy. A priori estimation of memory effects in reduced-order models of nonlinear systems using the Mori–Zwanzig formalism. *Proceedings of the Royal Society A*, 473(2205):20170385, 2017.

- [34] E. Hairer, S. P. N̄rsett, and G. Wanner. *Solving ordinary differential equations I*. Springer Berlin Heidelberg, 1993.
- [35] P. Holmes, J. L. Lumley, G. Berkooz, and C. W. Rowley. *Turbulence, coherent structures, dynamical systems and symmetry*. Cambridge university press, 2012.
- [36] W. Hundsdorfer and J. G. Verwer. *Numerical solution of time-dependent advection-diffusion-reaction equations*, volume 33. Springer Science & Business Media, 2013.
- [37] J. W. Hurrell, M. M. Holland, P. R. Gent, S. Ghan, J. E. Kay, P. J. Kushner, J.-F. Lamarque, W. G. Large, D. Lawrence, K. Lindsay, et al. The community earth system model: a framework for collaborative research. *Bulletin of the American Meteorological Society*, 94(9):1339–1360, 2013.
- [38] A. A. Keller. Generalized delay differential equations to economic dynamics and control. *American-Math*, 10:278–286, 2010.
- [39] G. Koch, W. Krzyzanski, J. J. Pérez-Ruixo, and J. Schropp. Modeling of delays in PKPD: classical approaches and a tutorial for delay differential equations. *Journal of pharmacokinetics and pharmacodynamics*, 41(4):291–318, 2014.
- [40] D. Kondrashov, M. D. Chekroun, and M. Ghil. Data-driven non-Markovian closure models. *Physica D: Nonlinear Phenomena*, 297:33–55, 2015.
- [41] Y. Kuang. *Delay differential equations: with applications in population dynamics*. AP, 1993.
- [42] C. S. Kulkarni, A. Gupta, and P. F. Lermusiaux. Sparse regression and adaptive feature generation for the discovery of dynamical systems. In *International Conference on Dynamic Data Driven Application Systems*, pages 208–216. Springer, 2020.
- [43] K. Kunisch. Approximation schemes for the linear-quadratic optimal control problem associated with delay equations. *SIAM Journal on Control and Optimization*, 20(4):506–540, 1982.
- [44] J. N. Kutz, S. L. Brunton, B. W. Brunton, and J. L. Proctor. *Dynamic mode decomposition: data-driven modeling of complex systems*. SIAM, 2016.
- [45] S. Laizet, J. Nedić, and C. Vassilicos. Influence of the spatial resolution on fine-scale features in DNS of turbulence generated by a single square grid. *International Journal of Computational Fluid Dynamics*, 29(3-5):286–302, 2015.
- [46] P. F. J. Lermusiaux. Adaptive modeling, adaptive data assimilation and adaptive sampling. *Physica D: Nonlinear Phenomena*, 230(1):172–196, 2007. doi: 10.1016/j.physd.2007.02.014.
- [47] P. F. J. Lermusiaux, C. Evangelinos, R. Tian, P. J. Haley, Jr, J. J. McCarthy, N. M. Patrikalakis, A. R. Robinson, and H. Schmidt. Adaptive coupled physical and biogeochemical ocean predictions: A conceptual basis. In *Computational Science - ICCS 2004*, volume 3038 of *Lecture Notes in Computer Science*, pages 685–692. Springer Berlin Heidelberg, 2004. ISBN 978-3-540-22116-6. doi: 10.1007/978-3-540-24688-6\89.
- [48] P. F. J. Lermusiaux, C.-S. Chiu, G. G. Gawarkiewicz, P. Abbot, A. R. Robinson, R. N. Miller, P. J. Haley, Jr, W. G. Leslie, S. J. Majumdar, A. Pang, and F. Lekien. Quantifying uncertainties in ocean predictions. *Oceanography*, 19(1):92–105, 2006. doi: 10.5670/oceanog.2006.93.
- [49] P. F. J. Lermusiaux, P. Malanotte-Rizzoli, D. Stammer, J. Carton, J. Cummings, and A. M. Moore. Progress and prospects of U.S. data assimilation in ocean research. *Oceanography*, 19(1):172–183, 2006. doi: 10.5670/oceanog.2006.102.

- [50] P. F. J. Lermusiaux, P. J. Haley, W. G. Leslie, A. Agarwal, O. Logutov, and L. J. Burton. Multiscale physical and biological dynamics in the Philippine Archipelago: Predictions and processes. *Oceanography*, 24(1):70–89, 2011. doi: 10.5670/oceanog.2011.05. Special Issue on the Philippine Straits Dynamics Experiment.
- [51] M. Lesieur, O. Métais, P. Comte, et al. *Large-eddy simulations of turbulence*. Cambridge U. press, 2005.
- [52] J. Li and P. Stinis. Mori-zwanzig reduced models for uncertainty quantification. *Journal of Computational Dynamics*, 6(PNNL-SA-132853), 2019.
- [53] F. Los and M. Blaas. Complexity, accuracy and practical applicability of different biogeochemical model versions. *Journal of Marine Systems*, 81(1-2):44–74, 2010.
- [54] N. MacDonald and N. MacDonald. *Biological delay systems: linear stability theory*. Cambridge University Press, 2008.
- [55] K. Matsuya and M. Kanai. Exact solution of a delay difference equation modeling traffic flow and their ultra-discrete limit. *arXiv preprint arXiv:1509.07861*, 2015.
- [56] H. G. Matthies and M. Meyer. Nonlinear galerkin methods for the model reduction of nonlinear dynamical systems. *Computers & Structures*, 81(12):1277–1286, 2003.
- [57] R. Maulik and O. San. Explicit and implicit les closures for burgers turbulence. *Journal of Computational and Applied Mathematics*, 327:12–40, 2018.
- [58] R. Maulik, A. Mohan, B. Lusch, S. Madireddy, P. Balaprakash, and D. Livescu. Time-series learning of latent-space dynamics for reduced-order model closure. *Physica D: Nonlinear Phenomena*, 405:132368, 2020.
- [59] R. M. May. *Stability and complexity in model ecosystems*, volume 1. Princeton U. press, 2019.
- [60] J. C. McWilliams. Submesoscale currents in the ocean. *Proceedings of the Royal Society A: Mathematical, Physical and Engineering Sciences*, 472(2189):20160117, 2016.
- [61] J. C. McWilliams. Submesoscale surface fronts and filaments: secondary circulation, buoyancy flux, and frontogenesis. *Journal of Fluid Mechanics*, 823:391, 2017.
- [62] E. Mizutani and S. E. Dreyfus. On complexity analysis of supervised MLP-learning for algorithmic comparisons. In *IJCNN’01. International Joint Conference on Neural Networks. Proceedings (Cat. No. 01CH37222)*, volume 1, pages 347–352. IEEE, 2001.
- [63] P. A. Newberger, J. S. Allen, and Y. H. Spitz. Analysis and comparison of three ecosystem models. *Journal of Geophysical Research: Oceans (1978–2012)*, 108(C3), 2003.
- [64] M. A. Nowak. *Evolutionary dynamics: exploring the equations of life*. Harvard U. press, 2006.
- [65] A. Paszke, S. Gross, F. Massa, A. Lerer, J. Bradbury, G. Chanan, T. Killeen, Z. Lin, N. Gimeshein, L. Antiga, et al. Pytorch: An imperative style, high-performance deep learning library. In *Advances in neural information processing systems*, pages 8026–8037, 2019.
- [66] S. Pawar, S. E. Ahmed, O. San, and A. Rasheed. Data-driven recovery of hidden physics in reduced order modeling of fluid flows. *Physics of Fluids*, 32(3):036602, 2020.
- [67] G. D. Portwood, P. P. Mitra, M. D. Ribeiro, T. M. Nguyen, B. T. Nadiga, J. A. Saenz, M. Chertkov, A. Garg, A. Anandkumar, A. Dengel, et al. Turbulence forecasting via neural ODE. *arXiv preprint arXiv:1911.05180*, 2019.
- [68] A. Quarteroni, G. Rozza, et al. *Reduced order methods for modeling and computational reduction*, volume 9. Springer, 2014.

- [69] C. Rackauckas, M. Innes, Y. Ma, J. Bettencourt, L. White, and V. Dixit. Diffeqflux.jl - A julia library for neural differential equations. *arXiv preprint arXiv:1902.02376*, 2019.
- [70] C. Rackauckas, Y. Ma, J. Martensen, C. Warner, K. Zubov, R. Supekar, D. Skinner, and A. Ramadhan. Universal differential equations for scientific machine learning. *arXiv preprint arXiv:2001.04385*, 2020.
- [71] C. Rackauckas et al. SciML Scientific Machine Learning Software. <https://sciml.ai/>.
- [72] H. Rasmussen, G. Wake, and J. Donaldson. Analysis of a class of distributed delay logistic differential equations. *Mathematical and computer modelling*, 38(1-2):123–132, 2003.
- [73] J.-P. Richard. Time-delay systems: an overview of some recent advances and open problems. *automatica*, 39(10):1667–1694, 2003.
- [74] A. R. Robinson and P. F. J. Lermusiaux. Data assimilation for modeling and predicting coupled physical–biological interactions in the sea. In A. R. Robinson, J. J. McCarthy, and B. J. Rothschild, editors, *Biological-Physical Interactions in the Sea*, volume 12 of *The Sea*, chapter 12, pages 475–536. John Wiley and Sons, New York, 2002.
- [75] A. R. Robinson, P. F. J. Lermusiaux, and N. Q. Sloan III. Data assimilation. In K. H. Brink and A. R. Robinson, editors, *The Global Coastal Ocean-Processes and Methods*, volume 10 of *The Sea*, chapter 20, pages 541–594. John Wiley and Sons, New York, 1998.
- [76] A. R. Robinson, P. J. Haley, P. F. J. Lermusiaux, and W. G. Leslie. Predictive skill, predictive capability and predictability in ocean forecasting. In *Proceedings of "The OCEANS 2002 MTS/IEEE" conference*, pages 787–794. Holland Publications, September 2002. doi: 10.1109/oceans.2002.1192070.
- [77] N. M. Robinson, W. A. Nelson, M. J. Costello, J. E. Sutherland, and C. J. Lundquist. A systematic review of marine-based species distribution models (SDMs) with recommendations for best practice. *Frontiers in Marine Science*, 4:421, 2017.
- [78] M. R. Roussel. The use of delay differential equations in chemical kinetics. *The journal of physical chemistry*, 100(20):8323–8330, 1996.
- [79] Y. Rubanova, R. T. Chen, and D. Duvenaud. Latent odes for irregularly-sampled time series. *arXiv preprint arXiv:1907.03907*, 2019.
- [80] P. Sagaut, S. Deck, and M. Terracol. *Multiscale and multiresolution approaches in turbulence: LES, DES and hybrid RANS/LES methods: applications and guidelines*. World Scientific, 2013.
- [81] O. San and R. Maulik. Neural network closures for nonlinear model order reduction. *Advances in Computational Mathematics*, 44(6):1717–1750, 2018.
- [82] T. P. Sapsis and P. F. J. Lermusiaux. Dynamical criteria for the evolution of the stochastic dimensionality in flows with uncertainty. *Physica D: Nonlinear Phenomena*, 241(1):60–76, 2012. doi: 10.1016/j.physd.2011.10.001.
- [83] T. Schneider, S. Lan, A. Stuart, and J. Teixeira. Earth system modeling 2.0: A blueprint for models that learn from observations and targeted high-resolution simulations. *Geophysical Research Letters*, 44(24):12–396, 2017.
- [84] H. L. Smith. *An introduction to delay differential equations with applications to the life sciences*, volume 57. Springer New York, 2011.
- [85] P. Stinis. Renormalized Mori–Zwanzig-reduced models for systems without scale separation. *Proceedings of the Royal Society A*, 471(2176):20140446, 2015.
- [86] F. Takens. Detecting strange attractors in turbulence. In *Dynamical systems and turbulence, Warwick 1980*, pages 366–381. Springer, 1981.

- [87] I. T. Tokuda, O. E. Akman, and J. C. Locke. Reducing the complexity of mathematical models for the plant circadian clock by distributed delays. *J. of theoretical biology*, 463:155–166, 2019.
- [88] M. P. Ueckermann and P. F. J. Lermusiaux. High order schemes for 2D unsteady biogeochemical ocean models. *Ocean Dynamics*, 60(6):1415–1445, Dec. 2010. doi: 10.1007/s10236-010-0351-x.
- [89] Z. Y. Wan, P. Vlachas, P. Koumoutsakos, and T. Sapsis. Data-assisted reduced-order modeling of extreme events in complex dynamical systems. *PloS one*, 13(5), 2018.
- [90] Q. Wang, N. Ripamonti, and J. S. Hesthaven. Recurrent neural network closure of parametric POD-galerkin reduced-order models based on the Mori-Zwanzig formalism. *Journal of Computational Physics*, page 109402, 2020.
- [91] Z. Wang, I. Akhtar, J. Borggaard, and T. Iliescu. Proper orthogonal decomposition closure models for turbulent flows: a numerical comparison. *CMAME*, 237:10–26, 2012.
- [92] B. A. Ward, M. Schartau, A. Oschlies, A. P. Martin, M. J. Follows, and T. R. Anderson. When is a biogeochemical model too complex? objective model reduction and selection for North Atlantic time-series sites. *Progress in Oceanography*, 116:49–65, 2013.
- [93] H. Whitney. Differentiable manifolds. *Annals of Mathematics*, pages 645–680, 1936.
- [94] C. Wunsch. *The ocean circulation inverse problem*. Cambridge University Press, 1996.
- [95] Y. Yang, M. Aziz Bhouri, and P. Perdikaris. Bayesian differential programming for robust systems identification under uncertainty. *Proceedings of the Royal Society A: Mathematical, Physical and Engineering Sciences*, 476(2243):20200290, 2020. doi: 10.1098/rspa.2020.0290.
- [96] P. Yeung, K. Sreenivasan, and S. Pope. Effects of finite spatial and temporal resolution in direct numerical simulations of incompressible isotropic turbulence. *Physical Review Fluids*, 3(6):064603, 2018.
- [97] J. Yuval, C. N. Hill, and P. A. O’Gorman. Use of neural networks for stable, accurate and physically consistent parameterization of subgrid atmospheric processes with good performance at reduced precision. *arXiv preprint arXiv:2010.09947*, 2020.

## Supplementary Information

## Neural Closure Models for Dynamical Systems

Abhinav Gupta\*<sup>1</sup> and Pierre F.J. Lermusiaux<sup>†1</sup><sup>1</sup>Department of Mechanical Engineering, Massachusetts Institute of Technology,  
Cambridge, MA 02139Sunday 17<sup>th</sup> July, 2022**1 Adjoint Equations for Neural Delay Differential Equations**

In this appendix, we provide a detailed derivation of adjoint equations for neural DDEs with discrete and distributed delays. For related derivations, we refer to [1, 2].

**1.1 Discrete-nDDE**

The neural-network parameterized discrete DDE is given by,

$$\begin{aligned} \frac{du(t)}{dt} &= f_{RNN}(u(t), u(t - \tau_1), \dots, u(t - \tau_K), t; \theta), \quad t \in (0, T] \\ u(t) &= h(t), \quad t \leq 0 \end{aligned} \quad (1)$$

where  $\tau_1, \dots, \tau_K$  are  $K$  number of discrete delays and  $f_{RNN}(\bullet; \theta)$  is any recurrent architecture with trainable parameters  $\theta$ . Let data be available at  $M$  times,  $T_1 < \dots < T_M \leq T$ . Our goal is to optimize the scalar loss function,  $\mathcal{L}(u(t)) = \int_0^T \sum_{i=1}^M l(u(t)) \delta(t - T_i) dt$  (where  $\delta(t)$  is the Kronecker delta function), given the data and nDDE.

We first start by writing the Lagrangian for the above system,

$$\begin{aligned} L = \mathcal{L}(u(t)) &+ \int_0^T \lambda^T(t) (d_t u(t) - f_{RNN}(u(t), u(t - \tau_1), \dots, u(t - \tau_K), t; \theta)) dt \\ &+ \int_{-\tau_K}^0 \mu^T(t) (u(t) - h(t)) dt \end{aligned} \quad (2)$$

where  $\lambda(t)$  and  $\mu(t)$  are the Lagrangian variables, and where, for brevity, we use  $\frac{\partial}{\partial(\bullet)} \equiv \partial(\bullet)$  and  $\frac{d}{d(\bullet)} = d(\bullet)$  from now on. We also assume that the loss function ( $\mathcal{L}$ ) and the initial conditions

\*guptaa@mit.edu

†pierrel@mit.edu

$(h(t), t \leq 0)$  are independent of  $\theta$ . Hence, the derivative of the Lagrangian w.r.t.  $\theta$  is given by,

$$\begin{aligned} d_\theta L = & \partial_{u(t)} \mathcal{L}(u(t)) d_\theta u(t) + \int_0^T \lambda^T (d_\theta d_t u(t) - \partial_{u(t)} f_{RNN}(\bullet, t; \theta) d_\theta u(t) u(t - \tau_1) \\ & - \partial_{u(t-\tau_1)} f_{RNN}(\bullet, t; \theta) d_\theta \dots - \partial_{u(t-\tau_K)} f_{RNN}(\bullet, t; \theta) d_\theta u(t - \tau_K) - \partial_\theta f_{RNN}(\bullet, t; \theta)) dt \quad (3) \\ & + \int_{-\tau_K}^0 \mu^T d_\theta u(t) dt. \end{aligned}$$

Using integration-by-parts, we can write,

$$\int_0^T \lambda^T d_\theta d_t u(t) dt = \lambda^T(T) d_\theta u(T) - \lambda^T(0) d_\theta u(0) - \int_0^T d_t \lambda^T(t) d_\theta u(t) dt \quad (4)$$

and by change of variables,

$$\begin{aligned} \int_0^T \lambda(t) \partial_{u(t-\tau_i)} f_{RNN}(\bullet, t; \theta) d_\theta u(t - \tau_i) dt \\ = \int_{-\tau_i}^{T-\tau_i} \lambda^T(t + \tau_i) \partial_{u(t-\tau_i)} f_{RNN}(\bullet, t + \tau_i; \theta) d_\theta u(t) dt \\ = \int_0^T \lambda^T(t + \tau_i) \partial_{u(t-\tau_i)} f_{RNN}(\bullet, t + \tau_i; \theta) d_\theta u(t) dt \\ + \int_{-\tau_i}^0 \lambda^T(t + \tau_i) \partial_{u(t-\tau_i)} f_{RNN}(\bullet, t + \tau_i; \theta) d_\theta u(t) dt \quad (5) \\ - \int_{T-\tau_i}^T \lambda^T(t + \tau_i) \partial_{u(t-\tau_i)} f_{RNN}(\bullet, t + \tau_i; \theta) d_\theta u(t) dt \\ = \int_0^T \lambda^T(t + \tau_i) \partial_{u(t-\tau_i)} f_{RNN}(\bullet, t + \tau_i; \theta) d_\theta u(t) dt \\ + \int_{-\tau_i}^0 \lambda^T(t + \tau_i) \partial_{u(t-\tau_i)} f_{RNN}(\bullet, t + \tau_i; \theta) d_\theta u(t) dt. \end{aligned}$$

We further assume  $\lambda(t) = 0, t \geq T$ . Inserting everything back into Eq. 3, we obtain,

$$\begin{aligned} d_\theta L = & \int_0^T \left( \sum_{i=1}^M \partial_{u(t)} l(u(t)) \delta(t - T_i) - d_t \lambda^T(t) - \lambda^T(t) \partial_{u(t)} f_{RNN}(\bullet, t; \theta) \right. \\ & \left. - \sum_{i=1}^K \lambda^T(t + \tau_i) \partial_{u(t-\tau_i)} f_{RNN}(\bullet, t + \tau_i; \theta) \right) d_\theta u(t) dt \quad (6) \\ & - \int_0^T \lambda^T(t) \partial_\theta f_{RNN}(\bullet, t; \theta) dt + \lambda^T(T) d_\theta u(T) - \lambda^T(0) d_\theta u(0) \\ & + \int_{-\tau_K}^0 \mu^T(t) d_\theta u(t) dt + \sum_{i=1}^K \int_{-\tau_i}^0 \lambda^T(t + \tau_i) \partial_{u(t-\tau_i)} f_{RNN}(\bullet, t + \tau_i) d_\theta u(t) dt \end{aligned}$$

The last term in the above equation is zero because of the user-defined initial condition are independent of  $\theta$ . Further, we aim to eliminate of  $d_\theta u(t)$  everywhere, because avoiding the need to compute it explicitly is the main premise of the adjoint method. We can do this if we assume,

$\mu(t) = \lambda(t)\delta(t)$  (where  $\delta(t)$  is the Kronecker delta function), and,

$$\begin{aligned} d_t \lambda^T(t) &= \sum_{i=1}^M \partial_{u(t)} l(u(t)) \delta(t - T_i) - \lambda^T(t) \partial_{u(t)} f_{RNN}(\bullet, t; \theta) \\ &\quad - \sum_{i=1}^K \lambda^T(t + \tau_i) \partial_{u(t-\tau_i)} f_{RNN}(\bullet, t + \tau_i; \theta), \quad t \in [0, T] \\ \lambda(t) &= 0, \quad t \geq T \end{aligned} \quad (7)$$

Finally, after solving the above adjoint equation in  $\lambda(t)$ , we can compute the required derivative  $d_\theta L$  as,

$$d_\theta L = - \int_0^T \lambda^T(t) \partial_\theta f_{RNN}(\bullet, t; \theta) dt \quad (8)$$

## 1.2 Distributed-nDDE

The neural network parameterized distributed DDE is given by,

$$\begin{aligned} \frac{du(t)}{dt} &= f_{NN} \left( u(t), \int_{t-\tau_2}^{t-\tau_1} g_{NN}(u(\tau); \phi) d\tau, t; \theta \right), \quad t \in (0, T] \\ u(t) &= h(t), \quad t \leq 0 \end{aligned} \quad (9)$$

where  $\tau_2 \geq \tau_1$  are the delay amounts; and  $f_{NN}(\bullet; \theta)$ ,  $g_{NN}(\bullet; \phi)$  are neural-networks with trainable parameters  $\theta$ ,  $\phi$  respectively. By introducing a new variable  $y(t) = \int_{t-\tau_2}^{t-\tau_1} g_{NN}(u(\tau); \phi) d\tau$ , we can rewrite the above equation as a coupled discrete DDEs,

$$\begin{aligned} \frac{du(t)}{dt} &= f_{NN}(u(t), y(t), t; \theta), \quad t \in (0, T] \\ \frac{dy(t)}{dt} &= g_{NN}(u(t - \tau_1); \phi) - g_{NN}(u(t - \tau_2); \phi), \quad t \in (0, T] \\ u(t) &= h(t), \quad \tau_2 \leq t \leq 0 \\ y(0) &= \int_{-\tau_2}^{-\tau_1} g_{NN}(h(t)) dt \end{aligned} \quad (10)$$

Also, let data be available at  $M$  times,  $T_1 < \dots < T_M \leq T$ . Our goal is to optimize the scalar loss function,  $\mathcal{L}(u(t)) = \int_0^T \sum_{i=1}^M l(u(t)) \delta(t - T_i) dt$ , given the data and nDDE.

We will again start by writing the Lagrangian for this setup,

$$\begin{aligned} L &= \mathcal{L}(u(t)) + \int_0^T \lambda^T(t) (d_t u(t) - f_{NN}(u(t), y(t), t; \theta)) dt \\ &\quad + \int_0^T \mu^T(t) (d_t y(t) - g_{NN}(u(t - \tau_1); \phi) + g_{NN}(u(t - \tau_2); \phi)) dt \\ &\quad + \int_{-\tau_2}^0 \gamma^T(t) (u(t) - h(t)) dt + \alpha^T \left( y(0) - \int_{-\tau_2}^{-\tau_1} g_{NN}(h(t)) dt \right), \end{aligned} \quad (11)$$

where  $\lambda(t)$ ,  $\mu(t)$ ,  $\gamma(t)$ , and  $\alpha$  are the Lagrangian variables. Now in this case, we need to obtain the

derivatives of the Lagrangian w.r.t. both  $\theta$  and  $\phi$ . We will first obtain  $d_\theta L$ ,

$$\begin{aligned}
d_\theta L = & \partial_{u(t)} \mathcal{L}(u(t)) d_\theta u(t) + \int_0^T \lambda^T(t) (d_\theta d_t u(t) - \partial_{u(t)} f_{NN}(\bullet, t; \theta) d_\theta u(t) - \partial_{y(t)} f_{NN}(\bullet, t; \theta) d_\theta y(t) \\
& - \partial_\theta f_{NN}(\bullet, t; \theta)) dt + \int_0^T \mu^T(t) (d_\theta d_t y(t) - \partial_{u(t-\tau_1)} g_{NN}(\bullet, t; \phi) d_\theta u(t - \tau_1) \\
& + \partial_{u(t-\tau_2)} g_{NN}(\bullet, t; \phi) d_\theta u(t - \tau_2)) dt + \int_{-\tau_2}^0 \gamma^T(t) d_\theta u(t) dt + \alpha^T d_\theta y(0).
\end{aligned} \tag{12}$$

Using integration-by-parts, we can write,

$$\begin{aligned}
\int_0^T \lambda^T(t) d_\theta d_t u(t) dt &= \lambda^T(T) d_\theta u(T) - \lambda^T(0) d_\theta u(0) - \int_0^T d_t \lambda^T(t) d_\theta u(t) dt \\
\int_0^T \mu^T(t) d_\theta d_t y(t) dt &= \mu^T(T) d_\theta y(T) - \mu^T(0) d_\theta y(0) - \int_0^T d_t \mu^T(t) d_\theta y(t) dt
\end{aligned} \tag{13}$$

and by change of variables,

$$\begin{aligned}
& \int_0^T \mu(t) \partial_{u(t-\tau_i)} g_{NN}(\bullet, t; \phi) d_\theta u(t - \tau_i) dt \\
&= \int_{-\tau_i}^{T-\tau_i} \mu^T(t + \tau_i) \partial_{u(t-\tau_i)} g_{NN}(\bullet, t + \tau_i; \phi) d_\theta u(t) dt \\
&= \int_0^T \mu^T(t + \tau_i) \partial_{u(t-\tau_i)} g_{NN}(\bullet, t + \tau_i; \phi) d_\theta u(t) dt \\
&\quad + \int_{-\tau_i}^0 \mu^T(t + \tau_i) \partial_{u(t-\tau_i)} g_{NN}(\bullet, t + \tau_i; \phi) d_\theta u(t) dt \tag{14} \\
&\quad - \int_{T-\tau_i}^T \mu^T(t + \tau_i) \partial_{u(t-\tau_i)} g_{NN}(\bullet, t + \tau_i; \phi) d_\theta u(t) dt \\
&= \int_0^T \mu^T(t + \tau_i) \partial_{u(t-\tau_i)} g_{NN}(\bullet, t + \tau_i; \phi) d_\theta u(t) dt \\
&\quad + \int_{-\tau_i}^0 \mu^T(t + \tau_i) \partial_{u(t-\tau_i)} g_{NN}(\bullet, t + \tau_i; \phi) d_\theta u(t) dt
\end{aligned}$$

We further assume  $\mu(t) = 0$ ,  $t \geq T$ . Inserting everything back (along with Eq. 5) into Eq. 12, we

obtain,

$$\begin{aligned}
d_\theta L = & \int_0^T \left( \sum_{i=1}^M \partial_{u(t)} l(u(t)) \delta(t - T_i) - d_t \lambda^T(t) - \lambda^T(t) \partial_{u(t)} f_{NN}(\bullet, t; \theta) \right. \\
& \left. - \mu^T(t + \tau_1) \partial_{u(t-\tau_1)} g_{NN}(\bullet, t + \tau_1; \phi) + \mu^T(t + \tau_2) \partial_{u(t-\tau_2)} g_{NN}(\bullet, t + \tau_2; \phi) \right) d_\theta u(t) dt \\
& - \int_0^T \lambda^T(t) \partial_\theta f_{NN}(\bullet, t; \theta) dt + \int_0^T (-d_t \mu^T(t) - \lambda^T(t) \partial_{y(t)} f_{NN}(\bullet, t; \theta)) d_\theta y(t) dt \\
& + \int_{-\tau_2}^0 (\gamma^T(t) - \lambda^T(t) \delta(t)) d_\theta u(t) dt + (\alpha^T - \mu^T(0)) d_\theta y(0) + \lambda^T(T) d_\theta u(T) + \mu^T(T) d_\theta y(T) \\
& - \int_{-\tau_1}^0 \mu^T(t + \tau_1) \partial_{u(t-\tau_1)} g_{NN}(\bullet, t + \tau_1; \phi) d_\theta u(t) dt \\
& + \int_{-\tau_2}^0 \mu^T(t + \tau_2) \partial_{u(t-\tau_2)} g_{NN}(\bullet, t + \tau_2; \phi) d_\theta u(t) dt
\end{aligned} \tag{15}$$

Again, the objective is to avoid the need to compute  $d_\theta u(t)$  and  $d_\theta y(t)$ , hence we assume,  $\mu(t) = 0$ ,  $t \geq T$ ;  $\lambda(T) = 0$ ;  $\gamma^T(t) = \lambda^T(t) \delta(t)$ ; and  $\alpha^T = \mu^T(0)$ . Keeping in mind that the initial condition  $h(t)$  is independent of  $\theta$ , we can write the following coupled adjoint equations,

$$\begin{aligned}
d_t \lambda^T(t) = & \sum_{i=1}^M \partial_{u(t)} l(u(t)) \delta(t - T_i) - \lambda^T(t) \partial_{u(t)} f_{NN}(\bullet, t; \theta) \\
& - \mu^T(t + \tau_1) \partial_{u(t-\tau_1)} g_{NN}(\bullet, t + \tau_1; \phi) \\
& + \mu^T(t + \tau_2) \partial_{u(t-\tau_2)} g_{NN}(\bullet, t + \tau_2; \phi), \quad t \in [0, T] \\
d_t \mu^T(t) = & - \lambda^T(t) \partial_{y(t)} f_{NN}(\bullet, t; \theta), \quad t \in [0, T] \\
\lambda^T(t) = & 0 \quad \text{and} \quad \mu^T(t) = 0, \quad t \geq T
\end{aligned} \tag{16}$$

Finally after solving the coupled adjoint equations in  $\lambda(t)$  and  $\mu(t)$ , we can compute the required derivative,  $d_\theta L$  as,

$$d_\theta L = - \int_0^T \lambda^T(t) \partial_\theta f_{NN}(\bullet, t; \theta) dt. \tag{17}$$

Now, to find  $d_\phi L$ , if we repeat the same procedure as shown above for  $\phi$ , we obtain exactly the same coupled adjoint equations (Eq. 16). Hence, once we solve the adjoint equations, we can also compute  $d_\phi L$  simultaneously as,

$$d_\phi L = - \int_0^T \mu^T(t) \partial_\phi g_{NN}(\bullet, t; \phi) dt. \tag{18}$$

## References

- [1] Andrew M Bradley. PDE-constrained optimization and the adjoint method. Technical report, Technical Report. Stanford University. <https://cs.stanford.edu/~ambrad>, 2013.
- [2] Jonathan Calver and Wayne Enright. Numerical methods for computing sensitivities for ODEs and DDEs. *Numerical Algorithms*, 74(4):1101–1117, 2017.